

# Doctoral Thesis

Physicochemical properties of poly(vinylidene fluoride)-based gel electrolytes with high Li salt concentration and their application in lithium batteries

(高濃度リチウム塩を含有するポリフッ化ビニリデン系ゲル電解質の物理化学特性とリチウム二次電池への応用)

Graduate School of Engineering Science

Yokohama National University

(横浜国立大学大学院 理工学府)

OCK Ji-Young

(玉 智英)

September 2021

**Physicochemical properties of poly(vinylidene fluoride)-based  
gel electrolytes with high Li salt concentration and their  
application in lithium batteries**

A Dissertation Submitted to Yokohama National University for  
the Partial Fulfillment of the Requirements for the Degree of  
Doctor of Engineering

**Submitted by**

Ock Ji-Young

18QB291

September 2021

Department of Chemistry and Life Science

Yokohama National University

Yokohama, Japan

## Content

Acknowledgement.....	6
Synopsis .....	8

### Chapter 1 General introduction

1.2 Electrolyte .....	13
1.2.1 Highly concentrated electrolyte .....	13
1.2.2 Inorganic electrolyte.....	16
1.2.3 Composite electrolyte.....	18
1.3 References .....	20

### Chapter 2 Preparation of PVDF–HFP gel electrolytes containing high concentration Li salts

2.1 PVDF–HFP gel electrolyte .....	29
2.1.1 Synthesis of PVDF–HFP gel electrolyte .....	29
2.2 Physical properties of gel electrolytes .....	30
2.2.1 Rheology test.....	30
2.2.2 Raman and XRD measurement.....	31
2.2.2 Ionic conductivity .....	33
2.3 Conclusions .....	34
2.4 References .....	35

### Chapter 3 Effects of anions in PVDF–HFP gel electrolytes containing high concentration Li salts on transport properties

3.1 Li ion conductivity of PVDF–HFP gel electrolyte .....	40
3.1.1 Li ion transference number .....	40
3.1.2 Li ion conductivity .....	42
3.2 Battery performance of PVDF–HFP gel electrolyte with [Li/LiCoO <sub>2</sub> ] cell .....	42
3.2.1 Rate performance of gel electrolytes .....	43
3.2.2 Li ion charge transfer resistance of a half cell of [Li/LiCoO <sub>2</sub> ].....	46
3.2.3 Voltage drop in the discharge curves.....	50
3.3 Conclusions .....	52
3.4 References .....	52

Chapter 4 Preparation of composite electrolytes composed of  
Li<sub>1.5</sub>Al<sub>0.5</sub>Ti<sub>1.5</sub>(PO<sub>4</sub>)<sub>3</sub> and PVDF–HFP gel electrolytes containing high  
concentration Li salts

4.1 Synthesis of LATP inorganic electrolyte and composite electrolyte....	58
4.1.1 Materials and experiments .....	59
4.2 Morphologies and mechanical properties of composite electrolytes....	60
4.2.1 Morphologies of composite electrolyte .....	61
4.2.2 Results of tensile measurements .....	63
4.3 Li ion exchange of composite electrolyte .....	64
4.3.1 Materials and experiments .....	65
4.3.2 Li ion exchange of composite electrolyte .....	66
4.4 Conclusions .....	69
4.5 References .....	69

Chapter 5 Electrochemical properties of Li<sub>1.5</sub>Al<sub>0.5</sub>Ti<sub>1.5</sub>(PO<sub>4</sub>)<sub>3</sub>/PVDF–HFP  
gel electrolyte

5.1 Rate performance of composite electrolytes.....	73
5.2 Ionic conductivity of composite electrolytes .....	75
5.3 Interfacial resistance at the interface of LATP and gel electrolyte.....	76
5.3.1 Experiments.....	76
5.3.2 Quantify the interfacial resistance of composite electrolyte.....	78
5.4 Conclusions .....	80
5.5 References .....	81

## Chapter 6. Concluding remarks and future directions

6. Concluding remarks and future directions.....	83
Publication list.....	85

## Acknowledgement

I am grateful to all those who contributed to me, and I wouldn't have made it through graduate school without them. Learning and adjusting was a big part of going abroad and the doctoral course was a challenge me to go but people in electrochemistry laboratory kept me going through it all. Over the past three years, I learn, grow and develop as a researcher by dint of their help and support.

My work would not have been possible without the thoughtful advices and unwavering support of my supervisor, Professor Kaoru Dokko. I would like to express my deepest gratitude and sincere appreciation to him, for his patience, thoughtful guidance, constructive suggestions and infinite support. I admire his profound insight into science and his ability to shape a story out of apparently meaningless data. It was an invaluable experience to get to be a student alongside him and I believe this experience remains a priceless asset and would certainly influence the whole of my life.

I would like to acknowledge members of my thesis committee, Professor Kaoru Dokko, Professor Masayoshi Watanabe, Professor Atobe Mahito, Professor Toshiyuki Oyama, Professor Naoaki Yabuuchi and Associate Professor Ueno Kazuhide, for their insightful suggestions on my final defense as well as my research. Their thoughtful advices and constructive comments on my final defense inspired me which way I should go as a researcher.

I really appreciate to Dr. Hishashi Kokubo, Dr. Kei Hashimoto, Dr. Jiali Liu and Dr. Ryoichi Tatara for their consideration and help. I admire Dr. Hishashi Kokubo for his thoughtful management of lab, which made a smooth way to research process for lab members. Dr. Kei Hashimoto, Dr. Jiali Liu and Dr. Ryoich Tatara are brilliant researchers, who helped me throughout my work. I spent plenty of time discussing science and life with Dr. Jiali Liu, and I am lucky to have her as friend. It's difficult to describe how grateful I am to have spent time working alongside them.

The colleagues and friends in our lab were also greatly influenced my work as a scientist. I really appreciate to Ms. Saiki Shiori, Mr. Shinji Kondou, Mr. Yosuke Ugata, Mr. Keisuke Shigenobu, Ms. Miki Fujishiro and other lab members for their

cooperation and considerable help for me. I learned how to properly operate and maintain the characterization tools from them. They never hesitate to help me and I truly appreciate their warm and invaluable help.

I would like to express my gratitude to Professor Izuru Kawamura, for his kind help in MAS-NMR measurements, which helped me a lot to have an insight into the composite electrolyte. I would like to appreciate the Ministry of Education, Culture, Sports, Science and Technology (MEXT) for financial support, to generously support me in the last three years.

Last but not least, I want to express all my love and gratitude to my family. I certainly couldn't make it this far if it weren't their consistent support and encouragement. I am deeply grateful to my mom and dad for always being there for me all the time.

## Synopsis

Rechargeable Lithium-ion batteries (LIB) have been extensively studied worldwide in recent decades to achieve the required energy demand. The classic LIBs are comprised of a transition-metal oxide cathode, carbon anode, and a nonaqueous electrolyte. Liquid electrolytes were found to have high ionic conductivity but inherently possess some disadvantages such as flammability, leakage and volatility problems. One of solutions to solve the safety issue with organic liquid electrolytes is using ionic liquids, which has low volatility, non-flammability and wide electrochemical window. Moreover, ionic liquids could be combined with polymer gel matrix and electrochemical properties can be controlled by molecular designing of the ionic liquid.

In this study, gel electrolytes composed of 30 wt% poly(vinylidene fluoride-co-hexafluoropropylene) (PVDF-HFP) and 70 wt% highly concentrated sulfolane (SL)-based electrolytes were prepared. It has been reported that Li ion hopping mechanism emerges in highly concentrated SL-based electrolytes, resulting in high Li ion conducting property with high thermal stability. By blending highly concentrated electrolytes and PVDF-HFP polymer network together, a flexible gel-type electrolyte having a high Li ion conducting ability were also prepared. The anionic effect of the SL-based gel electrolytes on the Li ion conductivity and charge transfer kinetics at the gel/electrode interface was studied. It is demonstrated that Li ion transport properties of gel electrolytes contribute to the Li/LiCoO<sub>2</sub> batteries, especially under high discharge current density where Li ions were involved in the severe electrochemical reaction at the electrode/electrolyte interface.

In addition, a flexible composite electrolyte was also prepared by combining NASICON (Sodium superionic conductor) type Li<sub>1.5</sub>Al<sub>0.5</sub>Ti<sub>1.5</sub>(PO<sub>4</sub>)<sub>3</sub> (LATP) oxide fillers and the gel electrolyte of [Li(SL)<sub>2</sub>][TFSA] through a solution casting

method. Replace the conventional liquid electrolytes into inorganic solid electrolytes is one way to settle the safety problem of lithium batteries. However, brittle and fragile nature of solid materials, which make the poor physical contact, are considered to be the origins of interfacial resistance at the electrode/electrolyte. To address these issues at the interfaces, many efforts have been devoted to prepare composite electrolytes combining inorganic solid electrolytes with polymer electrolytes. It was investigated the properties of the composite electrolytes composed of LATP and PVDF–HFP-gel such as mechanical properties, ion transport properties, electrochemical properties.

## **Chapter One**

### General introduction

## 1.1 Lithium-ion batteries

In 1976, M. Stanley Whittingham discovered the rechargeable battery that used the lithium metal as the anode and titanium disulfide intercalated with Li ion as the cathode.<sup>1</sup> Subsequently, layered oxide cathode ( $\text{LiCoO}_2$ ) was discovered that showed a high potential of 4-5 V to  $V_{\text{Li}}$  by John. B. Goodenough.<sup>2</sup> After Sony Corporation first announcement of the commercialization of lithium-ion battery in 1991, lithium-ion batteries have been extensively studied and developed worldwide in recent decades to achieve the required energy demand.<sup>3,4</sup>

Lithium-ion battery offers high energy densities because of the high theoretical capacity of lithium ( $3860 \text{ mA} \cdot \text{h} \cdot \text{g}^{-1}$ ) and generate a large potential difference when assembled with a transitional layered oxide material (**Figure 1-1**).<sup>5-7</sup> Therefore, Lithium-ion battery is one of the promising technologies for energy storage devices, and used in a wide range of power sources including portable electronic devices and electric vehicles.<sup>8-10</sup>

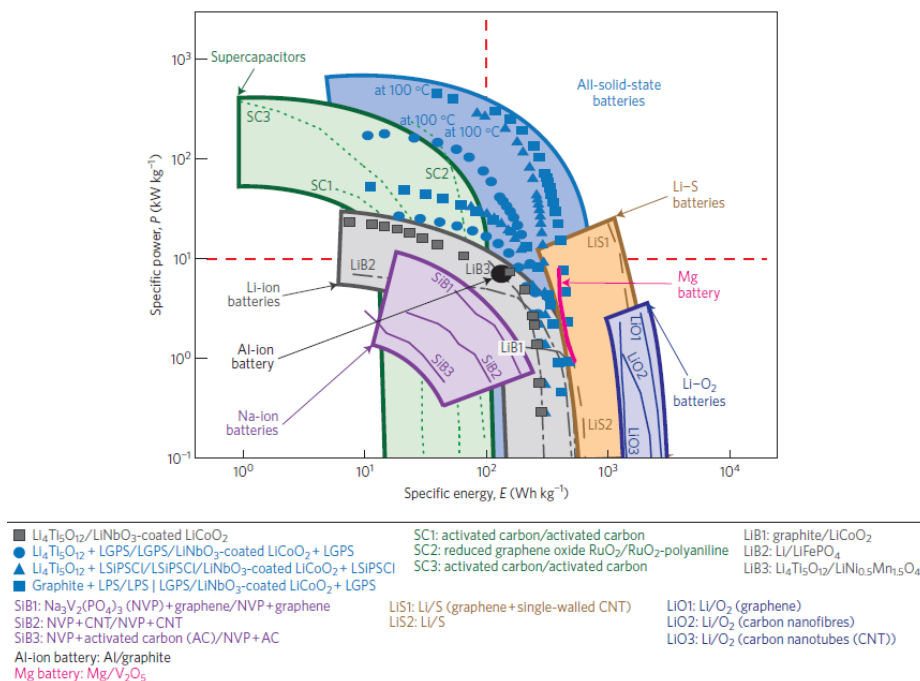


**Figure 1-1.** Comparison of different energy storage devices in terms of energy and power density. Adopted from ref. 11 with permission from the Springer Nature.

Generally, Li ion battery consists of an anode (negative electrode), cathode (positive electrode), electrolyte, separator and two current collectors (negative and positive).<sup>12-14</sup> During discharge, the anode released Li ions to the cathode, generating an electric current from one side to the other. The electrolyte carries Li ions through cell and Li ions insertion/extraction reaction occur in the electrode, which is accompanied by accepting an electron provided through the external circuit. To achieve the high energy and power density battery, the choice of cathode and anode with wide electrochemical window, as well as fast Li ion conductive electrolytes and good chemical stability is highly required.<sup>15</sup> **Figure 1-2** shows a schematic image and operating reaction of Li ion rechargeable battery. Typical electrode reaction of a LiCoO<sub>2</sub>/Graphite is described as follows.

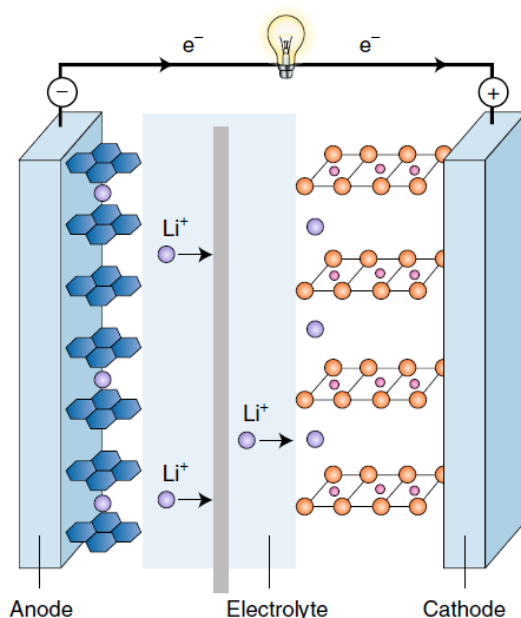
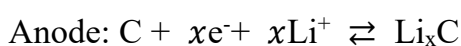
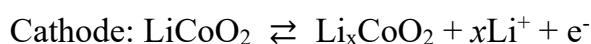


**Figure 1-2.** A schematic representation of a rechargeable Li-ion battery. Adopted

from ref. 16 with permission from the Springer Nature.

## 1.2 Electrolyte

Conventional organic electrolytes in lithium-ion batteries are typically a mixture of organic liquid electrolytes (e.g., ethylene carbonate (EC), diethyl carbonate (DEC), etc.) containing lithium salts (e.g., LiBF<sub>4</sub>, LiPF<sub>6</sub>, etc.).<sup>17,18</sup> Conventional organic electrolytes have high ionic conductivity on the order of 10<sup>-2</sup> S cm<sup>-1</sup> and could be penetrated porous electrode and provide good wettability; however, they have several disadvantages as well such as flammability, leakage, and volatility problems. Besides, both cations and anions are mobile in liquid electrolytes, resulting in an unwanted side reaction at the electrode/electrolyte interfaces, generation of salt concentration gradient during cell operation and limiting the cell performance especially at high current flow.<sup>19,20</sup>

A promising approach to address these issues with organic liquid electrolytes is to use highly concentrated electrolytes or solid electrolytes, which have low volatility, non-flammability, high ionic conductivity, high Li ion transference number and a wide electrochemical window.<sup>21</sup> Therefore, significant efforts have been made to demonstrate the applicability of solid electrolytes in Li secondary batteries and supercapacitors.

### 1.2.1 Highly concentrated electrolyte

Recently, highly concentrated electrolyte solutions containing Li salts have been widely investigated because of their attractive properties as electrolytes for Li batteries. Generally, in conventional liquid electrolyte ( $c_{Li} < 1 \text{ mol dm}^{-3}$ ), it contained considerable amount of free solvent and Li ion is assumed to be coordinated by solvent molecules and formation of solvent-separated ion pairs

(SSIPs) (**Figure 1-3a**).

As shown in **Figure 1-3b**, with increasing Li salt concentration, the Li ions competitively coordinated by the solvents and anions, resulting in the decline of free solvent species and formation of various complex ion associations from SSIPs to contact ion pairs (CIPs) and aggregate solvates (AGGs).<sup>22</sup> It should be noted that increasing Li salt concentration leads to the increase in the viscosity with a decrease in ionic conductivity.<sup>23</sup> Nevertheless, the highly concentrated electrolytes exhibit various attractive properties including low volatility, high transference number, wide electrochemical window, high thermal stability and improved redox stability, etc.<sup>24,25</sup> Combining the various cations and anions produced numerous highly concentrated electrolytes with different solvating structure and properties.<sup>26</sup>

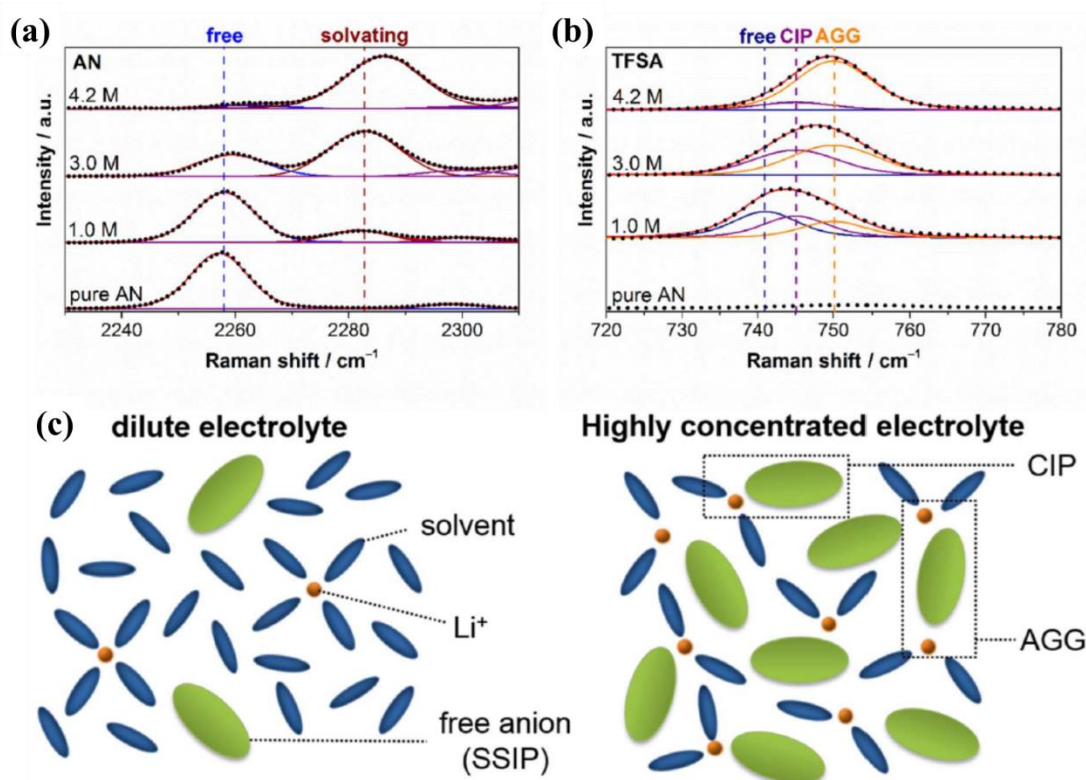


**Figure 1-3.** Raman spectra for a) acetonitrile (AN) solvents and b) [TFSA]<sup>-</sup> anions in LiTFSA/AN mixtures at various salt concentrations. c) Schematic images of typical coordination structures of a dilute solution ( $\sim 1 \text{ mol dm}^{-3}$ ) and a highly

concentrated solution ( $\sim 4.2 \text{ mol dm}^{-3}$ ). Adopted from ref. 23 with permission from the IOP Publishing.

Among these highly concentrated electrolytes, our group earlier reported highly concentrated sulfolane (SL)-based electrolytes that show remarkably  $\text{Li}^+$  transference numbers (0.7–0.8) and better rate performance of LIBs than that of the diluted liquid electrolyte.<sup>27,28</sup> In these highly concentrated SL-based electrolytes,  $\text{Li}^+$  ions are considered to be transferred via an anomalous ion-hopping/exchange mechanism, through which  $\text{Li}^+$  ions rapidly exchange ligands (solvent and anion) and travel in solvent- and anion-bridged Li-ion coordination clusters, as reflected by the fastest  $\text{Li}^+$  ion diffusion among the electrolyte components (**Figure 1-4**). Although SL-based electrolytes have low reductive (cathodic) stability and poor solid-electrolyte-interphase (SEI)-forming properties, highly concentrated LiFSA/SL electrolyte can show high coulombic efficiency (>99%) for Li deposition/dissolution cycles in a Li/Cu cell through the formation of a LiF layer at the electrolyte/Li metal interface.<sup>29–31</sup>

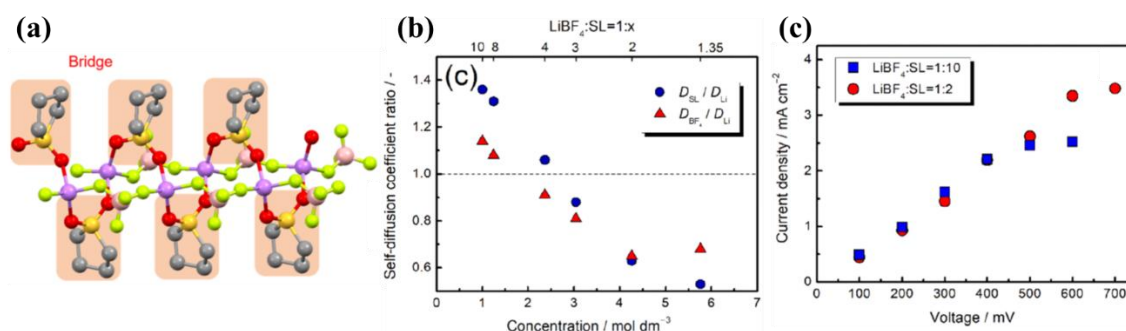


**Figure 1-4.** Sulfolane-based highly concentrated electrolytes Ball and stick model for  $\text{LiBF}_4/\text{SL} = 1:1$ , (b) ratios of self-diffusion coefficients of ion species of  $\text{LiBF}_4/\text{SL} = 1:1$  at  $30^\circ\text{C}$  and (c) dependency of steady-state current densities of Li symmetric cells with various applied voltage. Adopted from ref. 27 with permission from the American Chemical Society.

## 1.2.2 Inorganic electrolyte

Li-ion-conducting inorganic solid electrolytes (SEs) have been widely investigated because of their high thermal stability and single-ion conducting property.<sup>32</sup> As shown in **Figure 1-5**, many research has extensively investigated on the various crystal structures such as lithium superionic conductor (LISICON)-like, argyrodites, garnets, sodium superionic conductor (NASICON)-like, Li-Nitrides, Li-Hydrides, perovskites and Li-halides.<sup>33-44</sup> Sulfide-based SEs have shown high ionic conductivity in the order of  $10^{-3}$ – $10^{-2}$  S  $\text{cm}^{-1}$  at room temperature, comparable to that of conventional liquid electrolytes, and a Li-ion cell with a sulfide-based SE has been demonstrated to exhibit a high rate performance in a wide temperature range.<sup>45</sup>

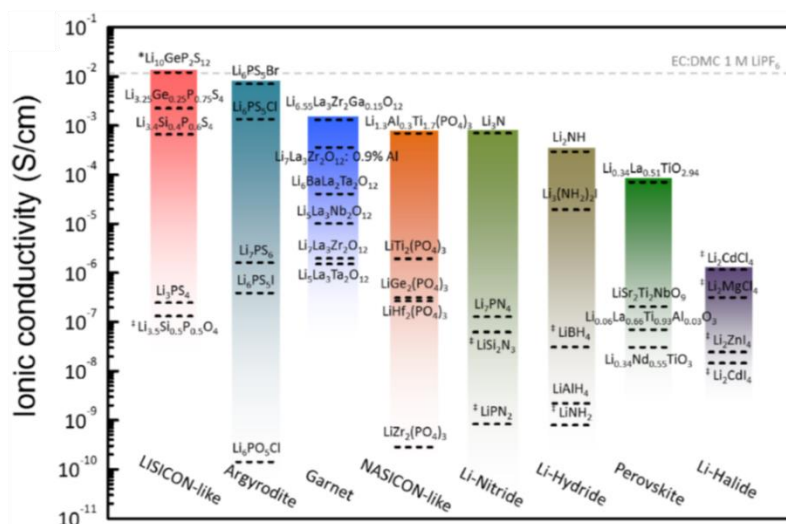


**Figure 1-5.** Reported total ionic conductivity of inorganic solid electrolytes at room temperature. Adopted from ref. 46 with permission from the American Chemical Society.

Generally, sulfide-based SEs react with moisture and require handling and cell assembly in an inert environment.<sup>47</sup> Recently, air stable sulfide electrolytes of As doped  $\text{Li}_4\text{SnS}_4$  were successfully synthesized by Liang and coworkers.<sup>48</sup> The lithium-ion conductivity could be greatly increased to  $1.39 \times 10^{-3} \text{ S cm}^{-1}$  at room temperature with substitution of Sn by As and showed superior air stability based on the rules of the hard and soft acids and bases (HSAB) theory, although the toxic nature of As ions made things challenging to use in practical battery application. Oxide-based SEs, such as  $\text{Li}_7\text{La}_3\text{Zr}_2\text{O}_{12}$  and  $\text{Li}_{1+x}\text{Al}_x\text{Ti}_{2-x}(\text{PO}_4)_3$  (LATP), have also been investigated because they have a higher chemical stability than their sulfide counterparts, although the ionic conductivity of oxide-based SEs is relatively low ( $\sim 10^{-4} \text{ S cm}^{-1}$ ) at room temperature.<sup>49-51</sup>

Many research groups have attempted to develop all-solid-state batteries with Li metal anode because of the high specific capacity of Li metal.<sup>6</sup> However, most inorganic SEs are thermodynamically unstable against Li metal and form decomposition phases, resulting in a narrow electrochemical window with high electrode–electrolyte interfacial resistance and deterioration in cell performance (**Figure 1-6a, b**).<sup>52-54</sup> The high resistance to  $\text{Li}^+$  conduction at the grain boundaries in oxide-based SEs is one of the reasons for the low conductivity. The surface roughness and brittleness of inorganic SEs, which make poor interfacial contact, are other reasons for the high interfacial resistance between the solid electrolyte and the electrode (**Figure 1-6c**).<sup>55,56</sup> In addition, there are many challenges in the manufacturing process of solid electrolyte sheets with a large area for use in practical Li-ion batteries.



be prepared using a feasible manner (Figure 1-7).<sup>68</sup>

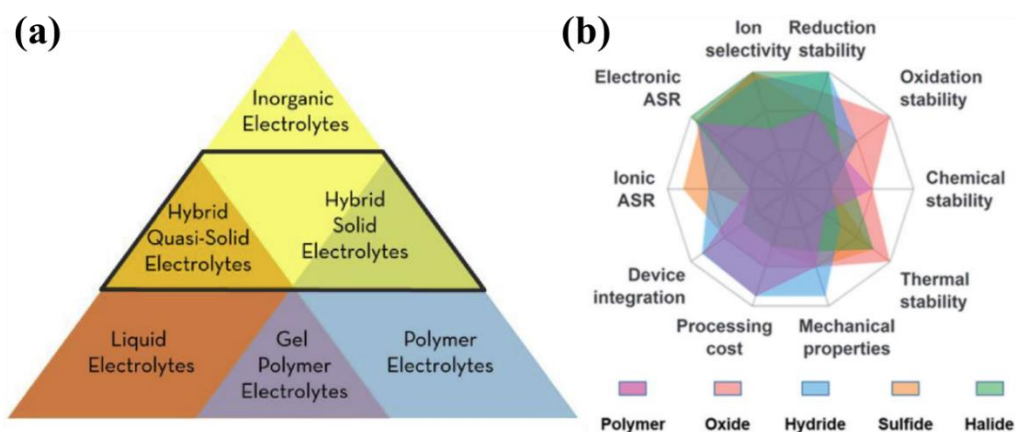


**Figure 1-7.** (a) Overview of single electrolytes and combination of these resulting in different types of hybrid electrolytes. Adopted from ref. 69 with permission from Elsevier. (b) The superposed plot of composite electrolytes with different types of solid electrolytes. Adopted from ref. 70 with permission from the Royal Society of Chemistry.

Incorporation of inorganic fillers into polymer matrix have been studied to improve the mechanical and electrochemical properties of the composite electrolytes: several kinds of passive fillers (e.g.,  $\text{TiO}_2$ ,  $\text{Al}_2\text{O}_3$ ,  $\text{SiO}_2$  etc.) or active fillers (e.g.,  $\text{Li}_{6.55}\text{Ga}_{0.15}\text{La}_3\text{Zr}_2\text{O}_{12}$  (LLZO),  $\text{Li}_{1.3}\text{Al}_{0.3}\text{Ti}_{1.7}(\text{PO}_4)_3$  (LATP),  $\text{LiZr}_2(\text{PO}_4)_3$  (LZP), etc.) have been examined so far.<sup>62,71–76</sup> Many attempts have been made to increase the ionic conductivity with morphology or size control of inorganic fillers in composite electrolytes. Compared with powder type inorganic fillers, interconnected inorganic fillers (e.g., fibers, wires, honeycomb, etc.) provide continuous Li ion transport pathway, which is believed to increase the ionic conductivity and transference number.<sup>62,63,77</sup>

Recently, quantitative evaluation of Li ion trace measurements in Poly(ethylene oxide) (PEO)/LLZO composite electrolytes was conducted by MAS-NMR and revealed the Li ion transport pathway in bulk electrolyte: at low volume fraction of LLZO, most of Li ion conduction promoted by segmental motion of PEO and LLZO served as passive fillers.<sup>78–80</sup> It is assumed that interaction between the inorganic fillers and polymer suppressed the crystallization of the polymer phase and increased amorphous regions in the composite electrolyte, leading to an enhancement of ionic conductivity. At high volume fraction of LLZO, LLZO fillers formed Li ion percolation pathway and Li ions mainly transport through the inorganic fillers. Based on these results, they suggested that Li ion conduction pathway is dominantly dependent on the main phase in the composite electrolytes, which is described with percolation threshold. The ionic conductivity enhancement is not attribute to the active fillers provide the Li ion transport pathway but because the interaction between inorganic fillers and polymer suppressed the crystallization of the polymer phase, suggest that active fillers actually work as passive fillers and difficult to achieve the synergistic effect on the ion transport property in the composites.<sup>81</sup>

### 1.3 References

- 1 M. S. Whittingham, *Science*, 1976, **192**, 1126–1127.
- 2 K. Mizushima, P. C. Jones, P. J. Wiseman and J. B. Goodenough, *Mater. Res. Bull.*, 1980, **15**, 783–789.
- 3 A. Yoshino, K. Sanechika and T. Nakajima, *US Pat. 4,668,595*, 1985
- 4 A. Yoshino, *Angew. Chemie - Int. Ed.*, 2012, **51**, 5798–5800.
- 5 X. Cheng, R. Zhang, C. Zhao and Q. Zhang, *Chem. Rev.*, 2017, **117**, 10403–10473.
- 6 T. Krauskopf, H. Hartmann, W. G. Zeier and J. Janek, *ACS Appl. Mater. Interfaces*, 2019, **11**, 14463–14477.
- 7 D. Lin, Y. Liu and Y. Cui, *Nat. Nanotechnol.*, 2017, **12**, 194–206.
- 8 B. Nykvist and M. Nilsson, 2015, **5**, 329–332.
- 9 A. Opitz, P. Badami, L. Shen, K. Vignarooban and A. M. Kannan, *Renew.*

- Sustain. Energy Rev.*, 2017, **68**, 685–692.
- 10 A. M. Andwari, A. Pesiridis, S. Rajoo, R. Martinez- and V. Esfahanian, *Renew. Sustain. Energy Rev.*, 2017, **78**, 414–430.
  - 11 Y. Kato, S. Hori, T. Saito, K. Suzuki, M. Hirayama, A. Mitsui, M. Yonemura, H. Iba and R. Kanno, *Nat. Energy*, 2016, **1**, 1–7.
  - 12 N. Nitta, F. Wu, J. T. Lee and G. Yushin, *Mater. Today*, 2015, **18**, 252–264.
  - 13 G. E. Blomgren, *J. Electrochem. Soc.*, 2017, **164**, A5019–A5025.
  - 14 A. Manthiram, *ACS Cent. Sci.*, 2017, **3**, 1063–1069.
  - 15 V. Etacheri, R. Marom, R. Elazari, G. Salitra and D. Aurbach, *Energy Environ. Sci.*, 2011, **4**, 3243–3262.
  - 16 J. B. Goodenough, *Nat. Electron.*, 2018, **1**, 204–204.
  - 17 D. Aurbach, *J. Power Sources*, 2000, **89**, 206–218.
  - 18 D. Aurbach, Y. Talyosef, B. Markovsky, E. Markevich, E. Zinigrad, L. Asraf, J. S. Gnanaraj and H. Kim, *Electrochim. Acta*, 2004, **50**, 247–254.
  - 19 K. Xu, *Chem. Rev.*, 2004, **104**, 4303–4418.
  - 20 K. Xu, *Chem. Rev.*, 2014, **114**, 11503–11618.
  - 21 M. Watanabe, M. L. Thomas, S. Zhang, K. Ueno, T. Yasuda and K. Dokko, 2017, **117**, 7190–7239.
  - 22 Y. Yamada, M. Yaegashi, T. Abe and A. Yamada, *Chem. Commun.*, 2013, **49**, 11194–11196.
  - 23 Y. Yamada and A. Yamada, *J. Electrochem. Soc.*, 2015, **162**, A2406–A2423.
  - 24 Y. Yamada, Y. Takazawa, K. Miyazaki and T. Abe, *J. Phys. Chem. C*, 2010, **114**, 11680–11685.
  - 25 Y. Yamada, K. Usui, C. H. Chiang, K. Kikuchi, K. Furukawa and A. Yamada, *ACS Appl. Mater. Interfaces*, 2014, **6**, 10892–10899.
  - 26 R. Hayes, G. G. Warr and R. Atkin, *Chem. Rev.*, 2015, **115**, 6357–6426.
  - 27 K. Dokko, D. Watanabe, Y. Ugata, M. L. Thomas, S. Tsuzuki, W. Shinoda, K. Hashimoto, K. Ueno, Y. Umebayashi and M. Watanabe, *J. Phys. Chem. B*, 2018, **122**, 10736–10745.
  - 28 A. Nakanishi, K. Ueno, D. Watanabe, Y. Ugata, Y. Matsumae, J. Liu, M. L. Thomas, K. Dokko and M. Watanabe, *J. Phys. Chem. C*, 2019, **123**, 14229–14238.
  - 29 X. Sun and C. A. Angell, *Electrochem. commun.*, 2005, **7**, 261–266.
  - 30 A. Abouimrane, I. Belharouak and K. Amine, *Electrochem. commun.*, 2009, **11**, 1073–1076.
  - 31 Y. Ugata, R. Tatara, T. Mandai, K. Ueno, M. Watanabe and K. Dokko, *ACS Appl. Energy Mater.*, 2021, **4**, 1851–1859.
  - 32 Y.-S. Hu, *Nat. Energy*, 2016, **1**, 1–2.
  - 33 H. Y. Hong, *Mater. Res. Bull.*, 1978, **13**, 117–124.
  - 34 U. V Alpen, M. F. Bell, W. Wichelhaus, K. Y. Cheung and G. J. Dudley,

- Electrochim. Acta*, 1976, **23**, 1395–1397.
- 35 H. Oguchi, M. Matsuo, T. Sato, H. Takamura, H. Maekawa, H. Kuwano and S. Orimo, *J. Appl. Phys.*, 2010, **107**, 096104.
- 36 H. D. Lutz, P. Kuske and K. Wussow, *Solid State Ionics*, 1988, **28–30**, 1282–1286.
- 37 A. R. Rodger, J. Kuwano and A. R. West, *Solid State Ionics*, 1985, **15**, 185–198.
- 38 H. Deiseroth, S. Kong, H. Eckert, J. Vannahme, C. Reiner, T. Zaiß and M. Schlosser, *Angew. Chemie - Int. Ed.*, 2008, **47**, 755–758.
- 39 M. Brinek, C. Hiebl and H. M. R. Wilkening, *Chem. Mater.*, 2020, **32**, 4754–4766.
- 40 V. Thangadurai, S. Narayanan and D. Pinzaru, *Chem. Soc. Rev.*, 2014, **43**, 4714–4727.
- 41 K. K. Fu, Y. Gong, B. Liu, Y. Zhu, S. Xu, Y. Yao, W. Luo, C. Wang, S. D. Lacey, J. Dai, Y. Chen, Y. Mo, E. Wachsman and L. Hu, *Sci. Adv.*, 2017, **3**, 1–12.
- 42 A. Hayashi, N. Masuzawa, S. Yubuchi, F. Tsuji, C. Hotehama, A. Sakuda and M. Tatsumisago, *Nat. Commun.*, 2019, **10**, 1–6.
- 43 A. Martínez-Juárez, C. Pecharrroma, J. E. Iglesias and M. J. Rojo, *J. Phys. Chem. B*, 1998, **102**, 372–375.
- 44 T. Lapp, S. Skaarup and A. Hooper, *Solid State Ionics*, 1983, **11**, 97–103.
- 45 N. Kamaya, K. Homma, Y. Yamakawa, M. Hirayama, R. Kanno, M. Yonemura, T. Kamiyama, Y. Kato, S. Hama, K. Kawamoto and A. Mitsui, *Nat. Mater.*, 2011, **10**, 2–6.
- 46 J. C. Bachman, S. Muy, A. Grimaud, H. H. Chang, N. Pour, S. F. Lux, O. Paschos, F. Maglia, S. Lupart, P. Lamp, L. Giordano and Y. Shao-Horn, *Chem. Rev.*, 2016, **116**, 140–162.
- 47 H. Muramatsu, A. Hayashi, T. Ohtomo, S. Hama and M. Tatsumisago, *Solid State Ionics*, 2011, **182**, 116–119.
- 48 G. Sahu, Z. Lin, J. Li, Z. Liu, N. Dudney and C. Liang, *Energy Environ. Sci.*, 2014, **7**, 1053–1058.
- 49 Q. Liu, Z. Geng, C. Han, Y. Fu, S. Li, Y. Bing He, F. Kang and B. Li, *J. Power Sources*, 2018, **389**, 120–134.
- 50 E. C. Bucharsky, K. G. Schell, A. Hintennach and M. J. Hoffmann, *Solid State Ionics*, 2015, **274**, 77–82.
- 51 H. Nakano, K. Dokko, M. Hara, Y. Isshiki and K. Kanamura, *Ionics*, 2008, **14**, 173–177.
- 52 P. Hartmann, T. Leichtweiss, M. R. Busche, M. Schneider, M. Reich, J. Sann, P. Adelhelm and J. Janek, *J. Phys. Chem. C*, 2013, **117**, 21064–21074.
- 53 Y. Zhu, X. He and Y. Mo, *ACS Appl. Mater. Interfaces*, 2015, **7**, 23685–23693.

- 54 S. Wenzel, T. Leichtweiss, D. Krüger, J. Sann and J. Janek, *Solid State Ionics*, 2015, **278**, 98–105.
- 55 R. D. Armstrong and R. A. Burnham, *J. Electroanal. Chem.*, 1976, **72**, 257–266.
- 56 H.-K. Tian and Y. Qi, *J. Electrochem. Soc.*, 2017, **164**, E3512–E3521.
- 57 Y. Zhu, X. He and Y. Mo, *ACS Appl. Mater. Interfaces*, 2015, **7**, 23685–23693.
- 58 W. D. Richards, L. J. Miara, Y. Wang, J. C. Kim and G. Ceder, *Chem. Mater.*, 2016, **28**, 266–273.
- 59 J. Janek and W. G. Zeier, *Nat. Energy*, 2016, **1**, 1–4.
- 60 P. Directorate and W. A. F. Base, *J. Power Sources*, 1994, **52**, 261–268.
- 61 S. Ali, C. Tan, M. Waqas, W. Lv, Z. Wei, S. Wu, B. Boateng, J. Liu, J. Ahmed, J. Xiong, J. B. Goodenough and W. He, *Adv. Mater. Interfaces*, 2018, **5**, 1–10.
- 62 T. Yang, J. Zheng, Q. Cheng, Y. Y. Hu and C. K. Chan, *ACS Appl. Mater. Interfaces*, 2017, **9**, 21773–21780.
- 63 L. Chen, Y. Li, S. P. Li, L. Z. Fan, C. W. Nan and J. B. Goodenough, *Nano Energy*, 2018, **46**, 176–184.
- 64 S. Yu, Q. Xu, C. Tsai, M. Ho, X. Lu, Q. Ma, H. Tempel, H. Kungl, H. Wiemho and R. Eichel, *ACS Appl. Mater. Interfaces*, 2020, **12**, 37067–37078.
- 65 M. Keller, A. Varzi and S. Passerini, *J. Power Sources*, 2018, **392**, 206–225.
- 66 M. Wirtz, H. Kungl, H. Tempel, P. Veelken, M. Linhorst, B. M. Moerschbacher and R. Eichel, 2020, 1–10.
- 67 N. Boaretto, L. Meabe, M. Martinez-ibañez, M. Armand and H. Zhang, *J. Electrochem. Soc.*, 2020, 167, 070524.
- 68 J. B. Goodenough and P. Singh, *J. Electrochem. Soc.*, 2015, 162, A2387–A2392.
- 69 M. Keller, A. Varzi and S. Passerini, *J. Power Sources*, 2018, **392**, 206–225.
- 70 T. Zhang, W. He, W. Zhang, T. Wang, P. Li, Z. Sun and X. Yu, *Chem. Sci.*, 2020, **11**, 8686–8707.
- 71 E. A. Rietman, M. L. Kaplan and R. J. Cava, *Solid State Ionics*, 1987, **25**, 41–44.
- 72 Z. Chen, P. A. Fitzgerald, G. G. Warr and R. Atkin, *Phys. Chem. Chem. Phys.*, 2015, **17**, 14872–14878.
- 73 W. Wang, E. Yi, A. J. Fici, R. M. Laine and J. Kieffer, *J. Phys. Chem. C*, 2017, **121**, 2563–2573.
- 74 C. W. Lin, C. L. Hung, M. Venkateswarlu and B. J. Hwang, *J. Power Sources*, 2005, **146**, 397–401.
- 75 S. Das and A. Ghosh, *AIP. Conf. Proc.*, 2016, **1731**, 110012.

- 76 Y. Li, B. Xu, H. Xu, H. Duan, X. Lü, S. Xin, W. Zhou, L. Xue, G. Fu, A. Manthiram and J. B. Goodenough, *Angew. Chemie - Int. Ed.*, 2017, **56**, 753–756.
- 77 W. Liu, N. Liu, J. Sun, P. Hsu, Y. Li, H. Lee and Y. Cui, *Nano Lett.*, 2015, 2740–2745.
- 78 J. Zheng and Y. Y. Hu, *ACS Appl. Mater. Interfaces*, 2018, **10**, 4113–4120.
- 79 J. Zheng, M. Tang and Y. Y. Hu, *Angew. Chemie - Int. Ed.*, 2016, **55**, 12538–12542.
- 80 J. Zheng, P. Wang, H. Liu and Y. Y. Hu, *ACS Appl. Energy Mater.*, 2019, **2**, 1452–1459.
- 81 J. Zheng, H. Dang, X. Feng, P. H. Chien and Y. Y. Hu, *J. Mater. Chem. A*, 2017, **5**, 18457–18463.

## **Chapter Two**

Preparation of PVDF–HFP gel electrolytes containing high  
concentration Li salts

Part of the work presented in this chapter has been published as: J. Ock, M. Fujishiro, K. Ueno, M. Watanabe, and K. Dokko, *Electrochemistry*, 2021, in press.

Combining an IL-based electrolyte with a polymer matrix to form polymer gel electrolytes can prevent electrolyte leakage and endow self-standing and flexible properties to the ILs.<sup>1-4</sup> In addition, the polymer gel electrolytes possess properties originating from ionic liquids such as high ionic conductivity, electrochemical stability, and nonflammability.<sup>3,5,6</sup> The electrochemical properties of a polymer gel electrolyte change depending on that of ionic liquid and can be controlled by molecular designing of the ionic liquid. Various polymers including Poly(ethylene oxide) (PEO), poly(acrylonitrile) (PAN), poly(methyl methacrylate) (PMMA) and poly(vinylidene fluoride) (PVDF) based polymer gel electrolytes have been extensively studied reported to date.<sup>7-13</sup>

Among polymer electrolytes, PVDF-based polymer matrix is often used to fabricate the polymer framework for polymer gel electrolytes. The PVDF–HFP polymer matrix is semicrystalline phase, which is known as the copolymers of PVDF with a number of HFP. The amorphous domains introduced by HFP components could uptake the liquid electrolytes and establish interesting physicochemical properties associated with combined liquid electrolytes.<sup>14-16</sup> In addition, the crystallinity of PVDF–HFP could be significantly reduced and plasticized by incorporation with liquid electrolytes, which could enhance the amorphous domains of the copolymer, resulting in a high IL uptake and a higher ionic conductivity on the order of  $10^{-4}$ – $10^{-3}$  S cm<sup>-1</sup> at room temperature. However, even highly ion-conductive IL-based gel electrolytes have a low Li ion transference number, a typical shortcoming of IL-based electrolytes, and poor Li-ion transport.<sup>17-19</sup>

Previous works have proposed using polymer gel electrolytes containing highly concentrated electrolytes as prospective solid-state electrolytes to simultaneously achieve fast Li<sup>+</sup> ion transport, high thermal stability, and a wide electrochemical

window (**Figure 2-1**).<sup>2,20</sup> A triblock copolymer of polystyrene-*b*-poly(methyl methacrylate)-*b*-polystyrene (PSt-*b*-PMMA-*b*-PSt, SMS) was combined with a tetraglyme (G4)-based highly concentrated electrolyte to provide a proof-of-concept for polymer gel electrolytes containing highly concentrated electrolytes, in which immiscible PSt segments form the physical cross-linking point of the polymer network and PMMA segments miscible with the electrolyte serve as an ion-conductive phase.

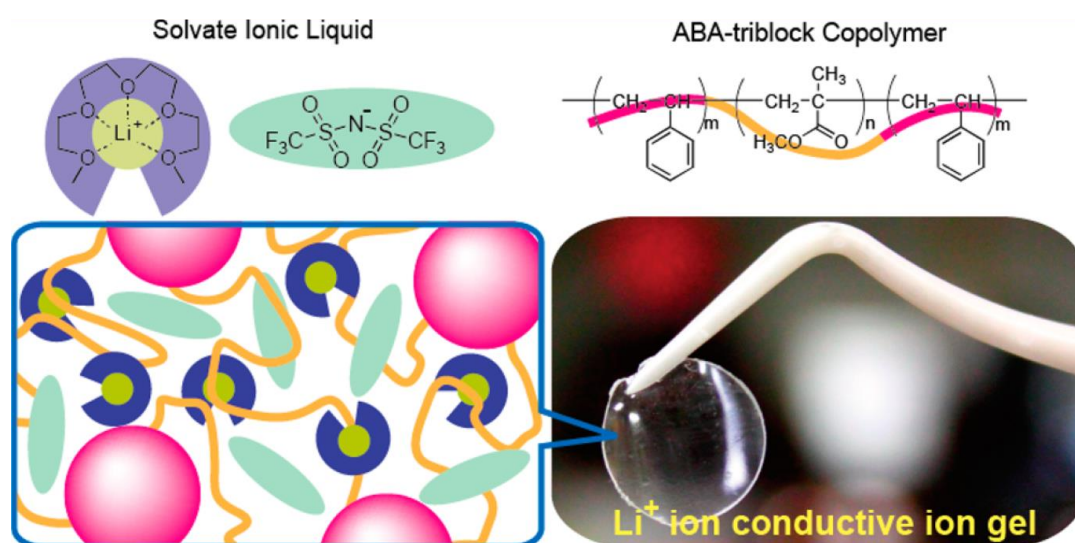


**Figure 2-1.** A triblock copolymer of polystyrene-*b*-poly(methyl methacrylate)-*b*-polystyrene (PSt-*b*-PMMA-*b*-PSt, SMS) polymer gel electrolytes containing [Li(G4)][TFSA] solvate ionic liquid. Adopted from ref. 20 with permission from the American Chemical Society.

In this chapter, we prepared gel electrolytes composed of commercially available PVDF–HFP and highly concentrated SL-based electrolytes in an attempt to enhance the Li-ion transport properties. The mechanical property of the gel polymer electrolytes with PVDF–HFP and SMS were examined through rheology test. Various Li salts such as LiN(SO<sub>2</sub>CF<sub>3</sub>)<sub>2</sub> (LiTFSA), LiN(SO<sub>2</sub>F)<sub>2</sub> (LiFSA), and LiBF<sub>4</sub> were used to investigate the anionic effects on the Li-ion conducting

properties. The obtained gels were further characterized by a series of techniques such as XRD and Raman, respectively.

## 2.1 PVDF–HFP gel electrolyte

### 2.1.1 Synthesis of PVDF–HFP gel electrolyte

#### Synthesis of highly concentrated electrolytes.

Purified SL, LiFSA and LiBF<sub>4</sub> were obtained from Kishida Chemical and used as received. LiTFSA was supplied by Solvay, Japan. The molar ratio of [LiTFSA]/[SL] = 1/2, [LiBF<sub>4</sub>]/[SL] = 1/2 and [LiFSA]/[SL] = 1/3 were chosen as electrolytes, which demonstrated fast Li ion conducting property and keep liquid state at room temperature. Purified G4 was purchased from Nippon Chemical and mixed with molar ratio of [LiTFSA]/[G4] = 1/1. The solvents and Li salts were mixed in a glove box filled with argon gas (VAC, [H<sub>2</sub>O] < 0.5 ppm) for overnight at room temperature until homogeneous liquid was obtained. The chemical structures were shown in **Figure 2-2**.

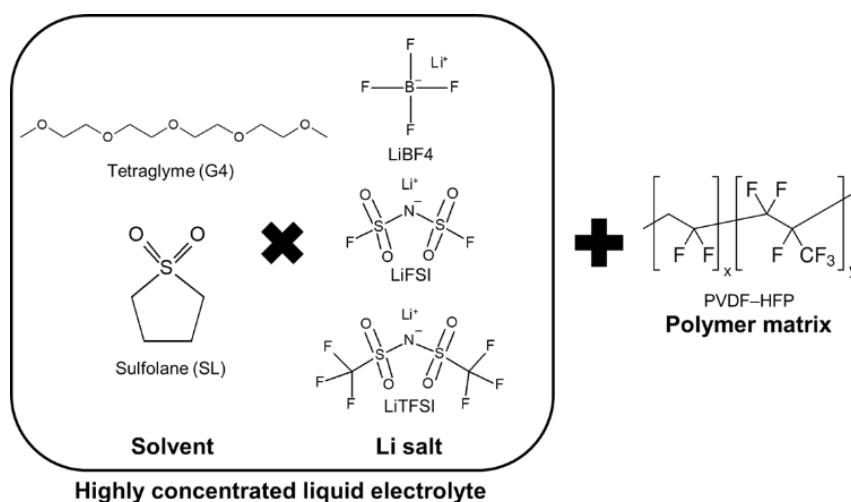


**Figure 2-2.** Chemical structures of solvents and Li salts employed in this study.

#### Making the gel membranes.

The membranes were processed inside dry chamber (HRG-60AR, Daikin, dew

point  $\sim -60$  °C). The polymer gel solutions of different highly concentrated electrolytes were prepared by dissolving the PVDF-*co*-HFP (Kynar flex 2801, Arkema) and [Li(G4)][TFSA], [Li(SL)<sub>2</sub>][TFSA], [Li(SL)<sub>2</sub>][BF<sub>4</sub>] and [Li(SL)<sub>3</sub>][FSA] into the anhydrous acetone (99 %, Sigma-Aldrich). The weight ratio of PVDF-*co*-HFP to highly concentrated electrolyte was fixed 3 to 7. The casting solution was stirred for 2 h and dried for overnight after pouring into a Petri dish. Afterwards, the gel membranes were peeled off and further vacuum dried at room temperature for overnight. The thickness of the gel membranes was in the range of 50–70  $\mu\text{m}$ .

## 2.2 Physical properties of gel electrolytes

### 2.2.1 Rheology test

The mechanical properties of gel membranes were compared with different polymer matrix. A plot of the moduli ( $G'$ ) as a function of dynamic stress amplitude for the [Li(G4)][TFSA] gel containing 30 wt% PVDF-HFP at 30 °C increased by an order of magnitude, compared to that of SMS contained gel, indicates a more rigid gel structure, as shown in **Figure 2-3**. The elastic shear moduli determined by oscillatory rheological measurements are  $\sim 6.4 \times 10^4$  and  $\sim 3.5 \times 10^4$  Pa for the [Li(SL)<sub>2</sub>][TFSA]/PVDF-HFP and [Li(G4)][TFSA]/PVDF-HFP gels, respectively—much higher than those for the previously reported [Li(G4)][TFSA]/SMS gel ( $\sim 5.9 \times 10^3$ ) with the same polymer content (30 wt%). This result suggests that PVDF-HFP yields a mechanically more robust polymer network than the SMS triblock copolymer (**Figure 2-3**), indicating that the gel has adequate mechanical properties to be flexible and self-standing.

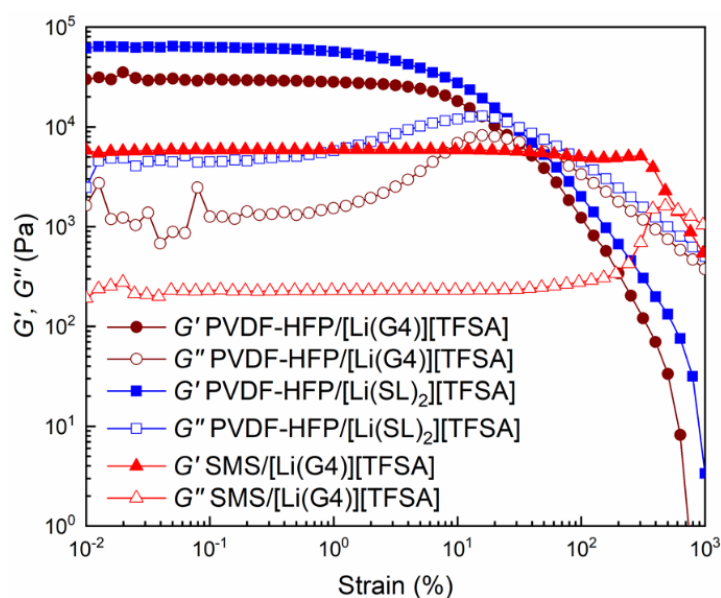


**Figure 2-3.** Elastic modulus as a function of dynamic stress amplitude of gel based on 70 wt% highly concentrated electrolytes in polymer matrix at 30 °C. The number-average molecular weight,  $M_n$ , of SMS is 39.7 kDa. The weight fraction of the PSt block,  $f_{PSt}$ , is 46.6 wt%.

## 2.2.2 Raman and XRD measurement

To investigate the Li ion coordination environment in the gel electrolyte, Raman spectroscopy was measured and Raman spectra of samples are shown in **Figure 2-4**. The Raman spectra for PVDF-HFP are greatly suppressed by mixing with  $[\text{Li}(\text{SL})_2][\text{TFSA}]$ , suggesting that gel was plasticized by incorporation with highly concentrated liquid electrolytes, which is already reported by elsewhere.<sup>17,18,21</sup> A new band at  $840\text{ cm}^{-1}$  of gel reflects the polar  $\beta$ -phase of PVDF-HFP, which is known to liquid electrolytes and salts promote the polar  $\beta$ -phase when mix with polymer matrix.<sup>15</sup> In general, the obtained spectra of gel resulted in a good match of the parent highly concentrated liquid electrolyte. The S–N stretching vibration of  $[\text{TFSA}]^-$  anions peak at around  $740\text{ cm}^{-1}$ , and monodentate and bridging type

SL solvent peak at around  $580\text{ cm}^{-1}$  are observed in the similar spectra in the presence of PVDF-HFP. Therefore, addition of PVDF-HFP lead to minor change on the local Li ion environment.<sup>20,22</sup>

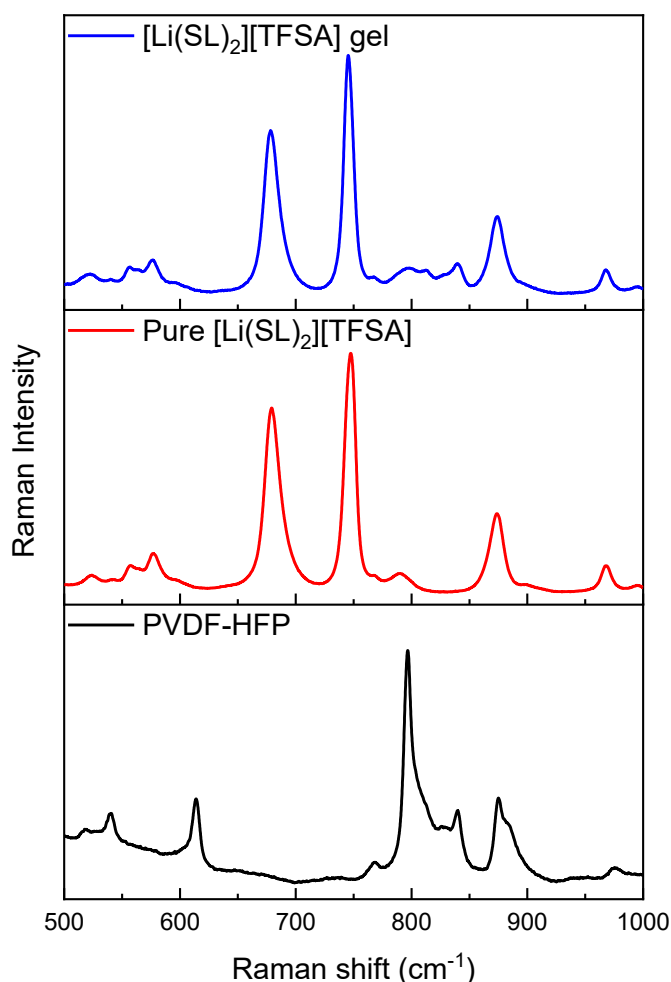


**Figure 2-4.** Raman result of  $[\text{Li}(\text{SL})_2][\text{TFSA}]$  gel membrane performed at room temperature.

The XRD patterns of PVDF-HFP, as shown in **Figure 2-5**, the XRD peaks could be indexed to crystalline  $\alpha$ -phase. In case of  $[\text{Li}(\text{SL})_2][\text{TFSA}]$  gel, the peaks of  $\alpha$ -phase were greatly broadened and reduced, indicating that the crystallinity of PVDF-HFP is significantly reduced and plasticized by incorporation with highly concentrated liquid electrolytes, as supported by Raman spectra in **Figure 2-4**.<sup>23</sup>

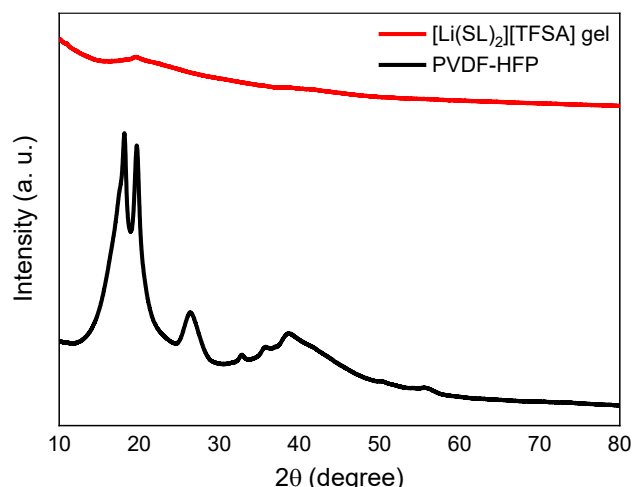


**Figure 2-5.** XRD measurement result of  $[\text{Li}(\text{SL})_2][\text{TFSA}]$  gel.

## 2.2.2 Ionic conductivity

The Arrhenius plots of the ionic conductivities of the gel electrolytes with different polymer matrix and highly concentrated electrolytes are shown in **Figure 2-6**. The ionic conductivity of the gel electrolytes is affected by the polymer matrix, as shown in **Figure 2-6a**. The  $[\text{Li}(\text{G4})][\text{TFSA}]/\text{PVDF-HFP}$  gel shows a higher ionic conductivity ( $3.1 \times 10^{-4} \text{ S cm}^{-1}$ ) than that of  $[\text{Li}(\text{G4})][\text{TFSA}]/\text{SMS}$  gel ( $1.7 \times 10^{-4} \text{ S cm}^{-1}$ ) at  $30 \text{ }^\circ\text{C}$ . This is probably because of the higher carrier density and mobility of the PVDF-HFP gel, owing to the lower volume fraction of the polymer matrix in the fluorinated PVDF-HFP gel electrolyte than that of the hydrocarbon-based SMS gel electrolyte. The ionic conductivities of the gel electrolytes with PVDF-HFP are shown in **Figure 2-6b**. The  $[\text{Li}(\text{SL})_2][\text{TFSA}]$  gel shows ionic conductivity of  $1.5 \times 10^{-4} \text{ S cm}^{-1}$  at  $30 \text{ }^\circ\text{C}$ , which is lower than that of pure  $[\text{Li}(\text{SL})_2][\text{TFSA}]$  ( $4.2 \times 10^{-4} \text{ S cm}^{-1}$ ). The decrease in the ionic carrier density and mobility in the presence of the polymer matrix is responsible for reduction in the

ionic conductivity of the gel electrolyte. The ionic conductivities of the gel electrolytes are in the order:  $[\text{Li}(\text{SL})_2][\text{TFSA}] < [\text{Li}(\text{SL})_2][\text{BF}_4] < [\text{Li}(\text{G4})][\text{TFSA}] < [\text{Li}(\text{SL})_3][\text{FSA}]$ ; this trend agrees well with the order of conductivity of the parent liquid electrolytes.<sup>24-26</sup> The highest conductivity ( $7.2 \times 10^{-4} \text{ S cm}^{-1}$ ) was obtained for the  $[\text{Li}(\text{SL})_3][\text{FSA}]$  gel. The higher content of SL in  $[\text{Li}(\text{SL})_3][\text{FSA}]$  afforded a higher ionic conductivity than that of  $[\text{Li}(\text{SL})_2][\text{TFSA}]$  and  $[\text{Li}(\text{SL})_2][\text{BF}_4]$ . Because  $[\text{Li}(\text{SL})_2][\text{FSA}]$  does not form a homogeneous liquid electrolyte owing to the higher melting point of the solid solvate  $[\text{Li}(\text{SL})_1][\text{FSA}]$ ,  $[\text{Li}(\text{SL})_3][\text{FSA}]$  is used to prepare the gel electrolyte in this study.

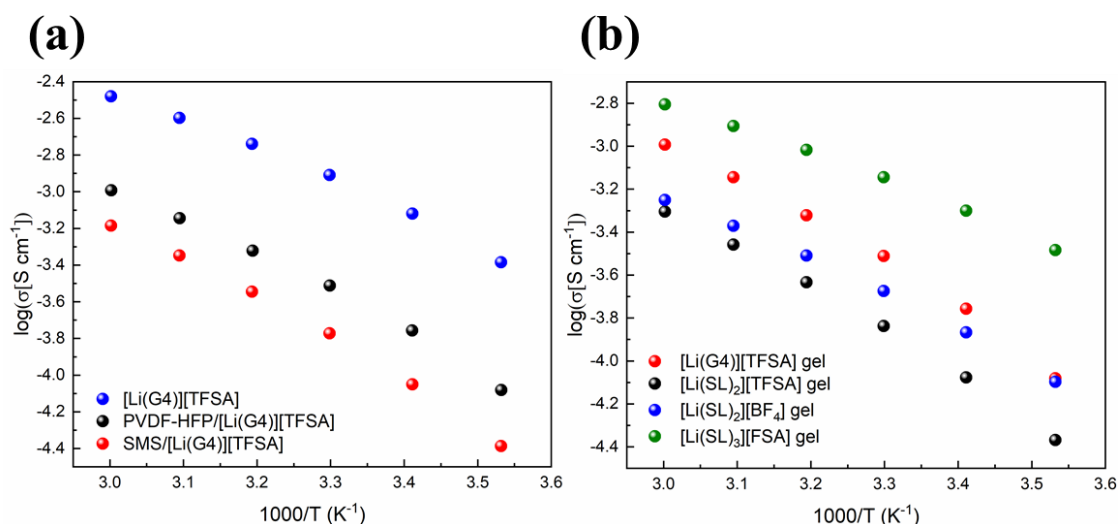


**Figure 2-6.** (a) Ionic conductivity of  $[\text{Li}(\text{G4})][\text{TFSA}]$  gel electrolytes with the different polymer matrix at the weight ratio of  $[\text{Li}(\text{G4})][\text{TFSA}]$  : polymer = 70 : 30. (b) Ionic conductivity of gel electrolytes with different highly concentrated electrolytes at a weight ratio of 70:30 (highly concentrated electrolyte : PVDF–HFP).

## 2.3 Conclusions

In this work, fast Li ion conductive gel electrolytes comprising PVDF–HFP and

highly concentrated electrolytes were prepared using a solution casting method. The elastic shear moduli of PVDF–HFP gel showed remarkable mechanical property of  $\sim 6.4 \times 10^4$  and  $\sim 3.5 \times 10^4$  Pa for the [Li(SL)<sub>2</sub>][TFSA]/PVDF–HFP and [Li(G4)][TFSA]/PVDF–HFP gels, respectively, indicating that PVDF–HFP matrix provide flexible network in the gel. The Raman spectra of gel correspond well with the parent highly concentrated electrolytes, indicating that the local Li ion coordination environment is maintained in the presence of the PVDF–HFP. The prepared SL based gel electrolytes showed sufficient conductivity as contained highly concentrated liquid electrolytes applicable to lithium batteries.

## 2.4 References

- 1 I. Osada, H. de Vries, B. Scrosati and S. Passerini, *Angew. Chemie - Int. Ed.*, 2016, **55**, 500–513.
- 2 Y. Kitazawa, K. Iwata, R. Kido, S. Imaizumi, S. Tsuzuki, W. Shinoda, K. Ueno, T. Mandai, H. Kokubo, K. Dokko and M. Watanabe, *Chem. Mater.*, 2018, **30**, 252–261.
- 3 X. Cheng, J. Pan, Y. Zhao, M. Liao and H. Peng, *Adv. Energy Mater.*, 2017, **8**, 1702184.
- 4 F. Zhao, Y. Shi, L. Pan and G. Yu, *Acc. Chem. Res.*, 2017, **50**, 1734–1743.
- 5 M. Armand, *Polymer*, 1983, **9–10**, 745–754.
- 6 A. M. Stephan, *Eur. Polym. J.*, 2006, **42**, 21–42.
- 7 D. M. Pesko, Y. Jung, A. L. Hasan, M. A. Webb, G. W. Coates, T. F. Miller and N. P. Balsara, *Solid State Ionics*, 2016, **289**, 118–124.
- 8 P. Tamilarasan and S. Ramaprabhu, *Energy*, 2013, **51**, 374–381.
- 9 S. Chandra, S. S. Sekhon and N. Arora, *Ionics*, 2000, **6**, 112–118.
- 10 E. Quartarone, C. Tomasi, P. Mustarelli, G. B. Appetecchi and F. Croce, *Electrochem. commun.*, 1998, **43**, 6–10.
- 11 Z. Xue, D. He and X. Xie, *J. Mater. Chem. A*, 2015, **3**, 19218–19253.
- 12 K. S. Ngai, S. Ramesh, K. Ramesh and J. C. Juan, *Ionics*, 2016, **22**, 1259–1279.
- 13 C. Liew, S. Ramesh and A. K. Arof, *Int. J. Hydrogen Energy*, 2013, **39**, 2953–2963.
- 14 S. K. Shalu, R. K. S. Chaurasia and S. Chandra, *J. Phys. Chem. B*, 2013, **117**, 897–906.
- 15 Y. Yang, S. Ramalingam, G. Wu, S. Ling, L. W. Kleiner, F. Tang, N. Ding and S. Hossainy, *Polymer*, 2008, **49**, 1926–1933.

- 16 R. E. Sousa, J. Nunes-pereira, J. C. C. Ferreira, C. M. Costa, A. V Machado, M. M. Silva and S. Lanceros-mendez, *Polym. Test.*, 2014, **40**, 245–255.
- 17 K. Elamin, M. Shojaatalhosseini, O. Danyliv, A. Martinelli and J. Swenson, *Electrochim. Acta*, 2019, **299**, 979–986.
- 18 S. Yeon, K. Kim, S. Choi, J. Cha and H. Lee, *J. Phys. Chem. B*, 2005, **109**, 17928–17935.
- 19 W. Liu, X. K. Zhang, F. Wu and Y. Xiang, *IOP Conf. Ser. Mater. Sci. Eng.*, 2017, **213**, 1–6.
- 20 Y. Kitazawa, K. Iwata, S. Imaizumi, H. Ahn, S. Y. Kim and K. Ueno, *Macromolecules*, 2014, **47**, 6009–6016.
- 21 T. Michot, A. Nishimoto and M. Watanabe, *Electrochim. Acta*, 2000, **45**, 1347–1360.
- 22 A. Nakanishi, K. Ueno, D. Watanabe, Y. Ugata, Y. Matsumae, J. Liu, M. L. Thomas, K. Dokko and M. Watanabe, *J. Phys. Chem. C*, 2019, **123**, 14229–14238.
- 23 A. Herzog-arbeitman, S. Maletti, S. Oswald, T. Schmeida, L. Giebeler and D. Mikhailova, *ACS Appl. Energy Mater.*, 2021, **4**, 1906–1914.
- 24 K. Dokko, D. Watanabe, Y. Ugata, M. L. Thomas, S. Tsuzuki, W. Shinoda, K. Hashimoto, K. Ueno, Y. Umebayashi and M. Watanabe, *J. Phys. Chem. B*, 2018, **122**, 10736–10745.
- 25 K. Ueno, K. Yoshida, M. Tsuchiya, N. Tachikawa, K. Dokko and M. Watanabe, *J. Phys. Chem. B*, 2012, **116**, 11323–11331.
- 26 K. Yoshida, M. Tsuchiya, N. Tachikawa, K. Dokko and M. Watanabe, *J. Phys. Chem. C*, 2011, **115**, 18384–18394.

## **Chapter Three**

Effects of anions in PVDF–HFP gel electrolytes containing high concentration Li salts on transport properties

Part of the work presented in this chapter has been published as: J. Ock, M. Fujishiro, K. Ueno, M. Watanabe, and K. Dokko, *Electrochemistry*, 2021, in press.

As a result of a growing demand for much safer, high energy and power density of energy storage system it is essential to achieve fast charge/discharge performance for accelerating the utility of electronic devices (e.g., electric vehicle, mobile phone, laptop, etc.).<sup>1-10</sup> The Li<sup>+</sup> ion charge transfer process in batteries involves the transport of the solvated Li<sup>+</sup> ion in the electrolyte and de(solvation) (or (de) intercalation) at the solid electrolyte interphase (SEI) and electrode/electrolyte interface by accepting an electron from the external circuit (**Figure 3-1a**).<sup>11-16</sup> In other words, electrochemical reactions proceed at the electrode/electrolyte interface, thus, a sufficient Li ion flux in bulk electrolyte with fast Li ion transfer at the electrode/electrolyte interface is crucial for achieving high power density.<sup>13,17-20</sup> To enhance the power performance of Lithium-ion batteries, especially at the rapid charge/discharge condition, it is important to achieve the high Li ion transference number with sufficient Li charge transfer rate at the electrode/electrolyte interface to suppress the concentration gradient and ensure the utilization of active materials (**Figure 3-1b**).

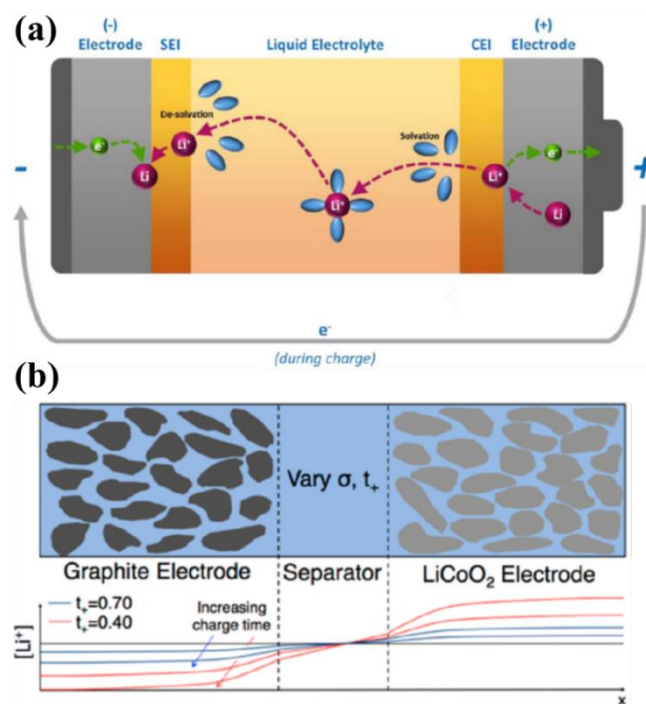


**Figure 3-1.** Schematic image of (a) Li ion charge transfer process in the cell during charge. Adopted from ref. 11 with permission from the IOP Publishing. (b) development of concentration gradient in the cell with various transference number. Adopted from ref. 21 with permission from the American Chemical Society.

In this chapter, AC impedance measurement, DC polarization, and galvanostatic charge/discharge cycling measurements were performed to evaluate the Li ion conducting property and interfacial resistance of the electrode/electrolyte with gel electrolytes. For further optimization of the gel electrolyte in Li secondary batteries, the anionic effects on the Li-ion conducting properties and interfacial resistance of the electrode/electrolyte were investigated using different Li salts such as LiTfSA, LiFSA and LiBF<sub>4</sub>. The gel electrolyte with the FSA anion exhibited high Li-ion conductivity and low charge transfer resistance at the electrode/electrolyte interface, and those are responsible for the better rate performance of Li/LiCoO<sub>2</sub> cells using the gel electrolyte.

## 3.1 Li ion conductivity of PVDF–HFP gel electrolyte

### 3.1.1 Li ion transference number

To determine the  $\text{Li}^+$  ion transference number ( $t_+$ ) of the gel electrolytes, a series of measurements of the electrochemical impedance and chronoamperometry of the same symmetric cell was performed at 30 °C. The  $\text{Li}^+$  ion transference number under anion-blocking conditions ( $t_+$ ) was calculated using the following equation developed by Bruce et al.<sup>22</sup>

$$t_+ = \frac{I_{ss}(\Delta V - I_{\Omega}R'_{0})}{I_{\Omega}(\Delta V - I_{ss}R'_{ss})}$$

where  $I_{\Omega}$  and  $I_{ss}$  are the initial and steady-state currents,  $R'_{0}$  and  $R'_{ss}$  are the initial and steady-state interfacial resistances, and  $\Delta V$  (10 mV in this work) is the DC potential drop across a symmetric cell. The initial current ( $I_{\Omega}$ ) was calculated using  $I_{\Omega} = \Delta V / (R'_{bulk} + R'_{0})$  (where  $R'_{bulk}$  is the resistance of the bulk electrolyte) based on Ohm's law, proposed by Balsara et al.<sup>23</sup>

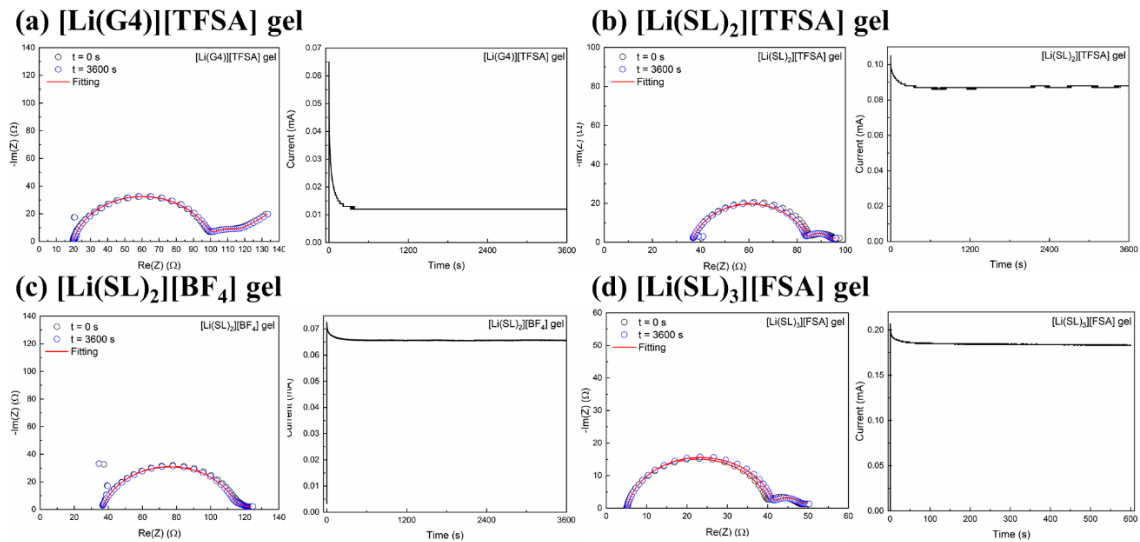


**Figure 3-2.** Nyquist plot of before/after polarization and polarization graph using

the [Li/Gel/Li] cell. The R-RC-RC-W equivalent circuit was used to fit the Li symmetric cell. The solid line represents a fit using individual equivalent circuit presented in above.

Gel electrolyte was sandwiched between two Li metal electrodes and measured by using a series of combination measurements with AC impedance and DC polarization method, shows the fitted Nyquist plot before/after polarization (**Figure 3-2** and **Table 3-3**), respectively. The  $t_+$  value is extremely low (0.03) for the [Li(G4)][TFSA] gel, whereas a much higher  $t_+$  (0.63) is obtained for the [Li(SL)<sub>2</sub>][TFSA] gel. These values primarily reflect the  $t_+$  values of the original liquid electrolytes, [Li(G4)][TFSA] (0.028) and [Li(SL)<sub>2</sub>][TFSA] (0.68).<sup>24</sup> Previous studies on dynamic ion correlations suggest that the substantially low  $t_+$  value of the [Li(G4)][TFSA] systems arises from the remarkable anti-correlations of ion motions under the constraint of momentum conservation of the ions.<sup>25,26</sup> [Li(SL)<sub>2</sub>][TFSA] has a high  $t_+$  value owing to the unique Li-ion hopping/exchange conduction in this highly concentrated electrolyte. All SL-based gel electrolytes showed relatively high transference number of > 0.5, especially with the [Li(SL)<sub>2</sub>][BF<sub>4</sub>] gel of 0.73, indicating the fast Li ion conducting promoted in case of SL-based gel electrolytes.<sup>27,28</sup>

**Table 3-3.** The fitting values of lithium transference numbers of the [Li/Gel/Li] cells determined by Bruce-Vincent-Evans method at 30 °C.

	Thickness [ $\mu\text{m}$ ]	$I_{\Omega}$ [mA]	$I_{ss}$ [mA]	$R'_{bulk}$ [ $\Omega$ ]	$R'_0$ [ $\Omega$ ]	$R'_{ss}$ [ $\Omega$ ]	$t_+$ [-]
[Li(G4)][TFSA]	76	0.080	0.012	19.4	88.1	88.4	0.03
[Li(SL) <sub>2</sub> ][TFSA]	71	0.106	0.088	36.6	56.1	56.0	0.65
[Li(SL) <sub>2</sub> ][BF <sub>4</sub> ]	73	0.072	0.066	35.9	82.9	81.4	0.73
[Li(SL) <sub>3</sub> ][FSA]	69	0.203	0.183	5.17	41.9	42.5	0.53

### 3.1.2 Li ion conductivity

The Li-ion conductivity can be estimated by multiplying the Li-ion transference number ( $t_+$ ) with the ionic conductivity. The ionic conductivity, Li transference number, and Li-ion conductivity of the gel electrolytes are summarized in **Table 3-4**.

**Table 3-4.** Ionic conductivity, Li<sup>+</sup> transference numbers and Li<sup>+</sup> conductivity of various gel electrolytes at 30 °C.

Electrolyte	Conductivity (S cm <sup>-1</sup> )	$t_+$	Li <sup>+</sup> conductivity ( $\sigma \times t_+$ ) (S cm <sup>-1</sup> )
[Li(G4)][TFSA]	$3.1 \times 10^{-4}$	0.03	$9.2 \times 10^{-6}$
[Li(SL) <sub>2</sub> ][TFSA]	$1.5 \times 10^{-4}$	0.65	$9.5 \times 10^{-5}$
[Li(SL) <sub>2</sub> ][BF <sub>4</sub> ]	$2.1 \times 10^{-4}$	0.73	$1.6 \times 10^{-4}$
[Li(SL) <sub>3</sub> ][FSA]	$7.2 \times 10^{-4}$	0.53	$3.8 \times 10^{-4}$

### 3.2 Battery performance of PVDF–HFP gel electrolyte with [Li/LiCoO<sub>2</sub>] cell

#### Battery performance

LiCoO<sub>2</sub> (AGC Seimi Chemical) and acetylene black (AB, DENKA) were used as received. LiCoO<sub>2</sub> (85 wt %), AB (9 wt %) as a carbon additive, and PVDF–HFP (6 wt %) as a polymer binder were mixed together and dispersed in *N*-methylpyrrolidone to prepare a slurry. The slurry was then spread on an Al current collector with a doctor blade and dried at 80 °C for over 2 h. The cathode sheet was punched into a circle (13.82 mm in diameter) and vacuum dried at 80 °C for over 2 h. The dried cathode, gel electrolyte, and Li metal anode were assembled in 2032-type coin cells. Next, 10  $\mu$ L of the highly concentrated electrolyte was added between the composite electrode and gel electrolyte. An aluminum-bodied cell was

used for the battery tests with the  $[\text{Li}(\text{SL})_3][\text{FSA}]$  gel electrolyte to avoid stainless steel corrosion.<sup>29</sup> The cells were assembled in a glovebox and aged at 30 °C for 12 h before testing. The typical mass loading of  $\text{LiCoO}_2$  on the Al foil was 3.2–3.3  $\text{mg cm}^{-2}$ . Galvanostatic charge–discharge measurements were conducted using an automatic charge–discharge machine (HJ1001SD8, Hokuto Denko) at 30 °C. The capacities and C rates were calculated based on mass loading in the  $\text{LiCoO}_2$  composite electrode. The electrochemical impedance spectra of a  $[\text{Li}/\text{gel}/\text{LiCoO}_2]$  cell were recorded at different potentials against the Li metal anode ( $V_{\text{Li}}$ ) in the range of 3.7–4.2  $V_{\text{Li}}$ . The cells were charged to a given potential at 0.2  $\text{mA cm}^{-2}$  with a rest period of 30 min. The impedance measurements were carried out with an amplitude of 10 mV in the frequency range of 1 MHz to 100 mHz.

### 3.2.1 Rate performance of gel electrolytes

$\text{Li}/\text{LiCoO}_2$  cells were assembled with gel electrolytes and galvanostatic charge–discharge tests were performed at 30 °C. **Figure 3-5** shows the discharge curves of the cells with  $[\text{Li}(\text{G4})][\text{TFSA}]$  gel (**Figure 3-5a**) and  $[\text{Li}(\text{SL})_2][\text{TFSA}]$  gel (**Figure 3-5b**) under various discharge current densities. The capacities and C rates are calculated based on the mass loading in the  $\text{LiCoO}_2$  composite electrode. At a current density of 0.2  $\text{mA cm}^{-2}$ , the discharge capacity of  $[\text{Li}(\text{G4})][\text{TFSA}]$  gel is only around 119  $\text{mA h g}^{-1}$ , while the  $[\text{Li}(\text{SL})_2][\text{TFSA}]$  gel showed 137  $\text{mA h g}^{-1}$ , which is close to the theoretical capacity (137  $\text{mA h g}^{-1}$ ) of  $\text{LiCoO}_2/\text{Li}_{0.5}\text{CoO}_2$ . Discharge curves at higher current densities show a more prominent difference. The cell with the  $[\text{Li}(\text{G4})][\text{TFSA}]$  gel delivers only 9  $\text{mA h g}^{-1}$  at 4  $\text{mA cm}^{-2}$ , one-tenth that of that delivered by the cell with the  $[\text{Li}(\text{SL})_2][\text{TFSA}]$  gel (94  $\text{mA h g}^{-1}$ ). The voltage drop in the early stage of discharge is significantly larger for the cell with the  $[\text{Li}(\text{G4})][\text{TFSA}]$  gel. In addition, the cell voltage in the middle and end of discharge decreases more steeply for the cell with the  $[\text{Li}(\text{G4})][\text{TFSA}]$  gel. These

results indicate that the  $[\text{Li}(\text{SL})_2][\text{TFSA}]$  gel shows better rate performance and lower internal resistance in the cell despite having a lower ionic conductivity. The internal resistance of the cells during discharge comprises the resistance for  $\text{Li}^+$  ion migration in the bulk electrolyte, the electronic and ionic resistances in the porous  $\text{LiCoO}_2$  cathode, the interfacial resistances at the  $\text{LiCoO}_2$  cathode and Li metal anode, and impedances for Li-ion diffusion in the electrolyte and the solid phase of  $\text{LiCoO}_2$ . One of the factors that accounts for the above difference in discharge rate capability is the Li-ion conductivity of the gel electrolyte. As shown in **Table 3-4**, Li ion conductivity for the  $[\text{Li}(\text{SL})_2][\text{TFSA}]$  gel at 30 °C increased by an order of magnitude, compared to that of  $[\text{Li}(\text{G4})][\text{TFSA}]$  gel, indicates the faster Li transport promoted in the bulk electrolyte and could further contribute to the improved cell performance.

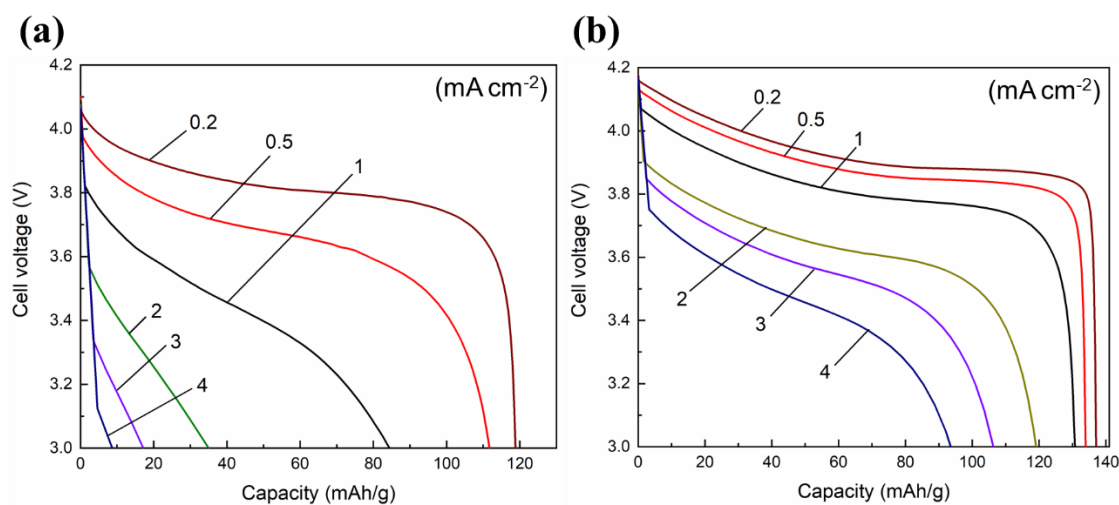


**Figure 3-5.** Discharge capacities of  $[\text{Li}/\text{Gel}/\text{LiCoO}_2]$  cells with (a)  $[\text{Li}(\text{G4})][\text{TFSA}]$  gel (thickness : 62  $\mu\text{m}$ ) and (b)  $[\text{Li}(\text{SL})_2][\text{TFSA}]$  gel (thickness : 62  $\mu\text{m}$ ) with various discharge current density at 30 °C. Full charge/discharge performance of the cells are in the **Figure 3-7**.

As can be seen in **Table 3-4**, the transference number of all the SL-based gel electrolytes is greater than 0.5, and the  $[\text{Li}(\text{SL})_2][\text{BF}_4]$  gel has the highest  $t_+$  value

(0.73). The  $[\text{Li}(\text{SL})_3][\text{FSA}]$  gel shows the highest Li-ion conductivity owing to the highest ionic conductivity and moderate  $t_+$  value among the studied gel electrolytes. Therefore, even better rate performance can be expected for the cell with the  $[\text{Li}(\text{SL})_3][\text{FSA}]$  gel electrolyte. **Figure 3-6** shows the discharge curves of the Li/LiCoO<sub>2</sub> cells with the  $[\text{Li}(\text{SL})_2][\text{BF}_4]$  (**Figure 3-6a**) and  $[\text{Li}(\text{SL})_3][\text{FSA}]$  gels (**Figure 3-6b**) at different discharge current densities. A comparison of the rate capability of the cells with the SL-based gel electrolytes is shown in **Figure 3-6c**. At a low current density of  $0.2 \text{ mA cm}^{-2}$ , all SL-based gel electrolytes allow high discharge capacities ( $\sim 137 \text{ mA h g}^{-1}$ ) with a high coulombic efficiency ( $>99.5\%$ ) (**Figure 3-7**). As the discharge current density increases, the discharge capacities of the cells gradually decrease along with an increase in the overpotential of discharge curves. At a high current density of  $13.3 \text{ mA cm}^{-2}$ , the cell with the  $[\text{Li}(\text{SL})_2][\text{TFSA}]$  gel retains almost no capacity, while that with the  $[\text{Li}(\text{SL})_2][\text{BF}_4]$  gel shows a low capacity ( $28 \text{ mA h g}^{-1}$ ) and a low coulombic efficiency (93.4%). However, the cell with the  $[\text{Li}(\text{SL})_3][\text{FSA}]$  gel shows a relatively high capacity ( $98 \text{ mA h g}^{-1}$ ) and a high coulombic efficiency (99.5%). On the basis of Li-ion conductivity (**Table 3-4**), it can be suggested that the electrolyte-derived ohmic drop and concentration polarization, which are more pronounced at higher current densities, increase in the order of  $[\text{Li}(\text{SL})_3][\text{FSA}] < [\text{Li}(\text{SL})_2][\text{BF}_4] < [\text{Li}(\text{SL})_2][\text{TFSA}]$ . Therefore, the Li-ion conductivity of the SL-based gel electrolytes significantly affects the rate performance of the cells.

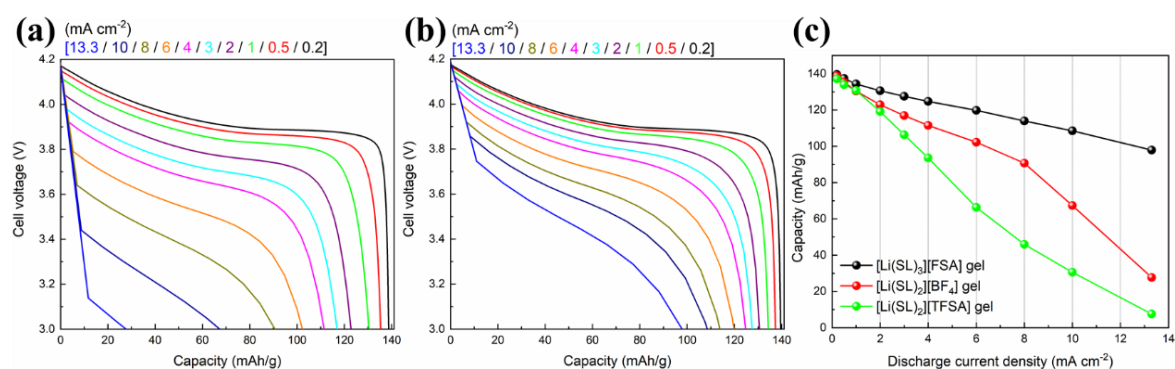


**Figure 3-6.** The 5<sup>th</sup> Discharge curves of [Li/Gel/LiCoO<sub>2</sub>] battery with different gel electrolytes of (a) [Li(SL)<sub>2</sub>][BF<sub>4</sub>] gel (thickness : 62 μm) and (b) [Li(SL)<sub>3</sub>][FSA] gel (thickness : 67 μm), respectively. (c) Discharge capacities of the cells with SL-based gel electrolytes as a function of current density. 1 C rate corresponds to ca. 0.46 mA cm<sup>-2</sup>.

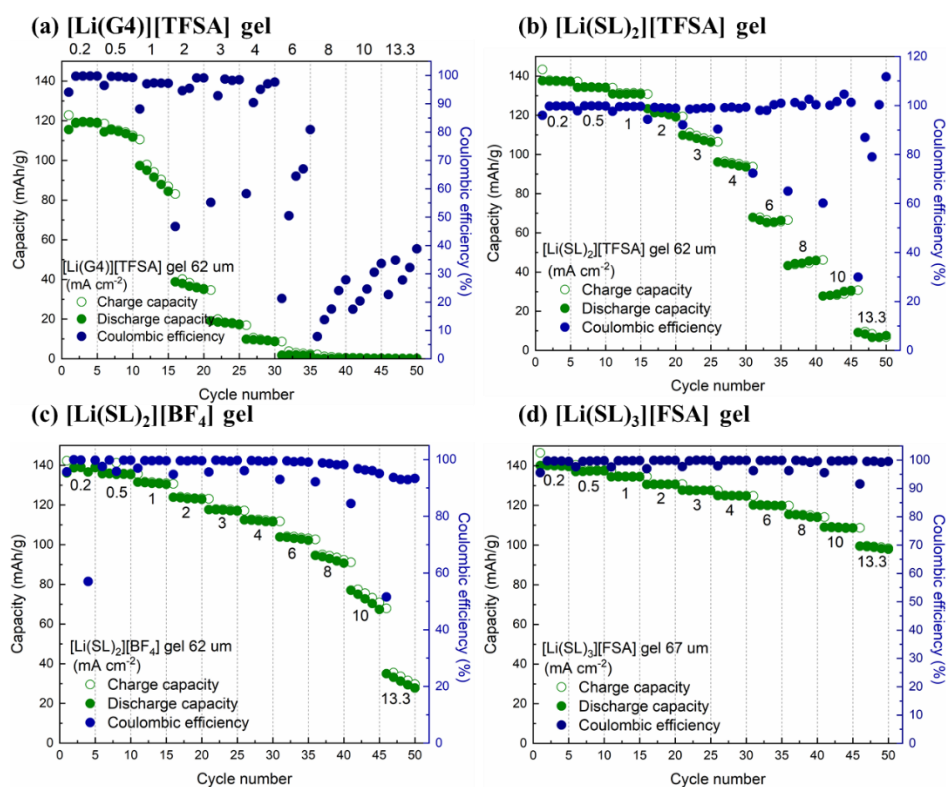


**Figure 3-7.** Rate performances of [Li/Gel/LiCoO<sub>2</sub>] battery with (a) [Li(G4)][TFSA], (b) [Li(SL)<sub>2</sub>][TFSA], (c) [Li(SL)<sub>2</sub>][BF<sub>4</sub>] and (d) [Li(SL)<sub>3</sub>][FSA] gel at different discharge current density (0.2 – 13.3 mA/cm<sup>2</sup>) at 30 °C.

### 3.2.2 Li ion charge transfer resistance of a half cell of [Li/LiCoO<sub>2</sub>]

In addition to the Li<sup>+</sup> ion transport process, the interfacial resistances for

electrochemical reactions can also be crucial factors affecting the power density of the cell. To study the interfacial resistances, electrochemical impedance spectroscopy (EIS) was performed on the Li/LiCoO<sub>2</sub> cells. Nyquist plots of the Li/LiCoO<sub>2</sub> cells with the gel electrolytes measured at 4.2 V<sub>Li</sub> are shown in **Figure 3-8**, and those measured at different voltages are depicted in **Figures 3-9**. In the two-electrode cell of Li/LiCoO<sub>2</sub>, charge transfer reactions occur at the Li metal anode and the LiCoO<sub>2</sub> cathode; therefore, the impedance of the cell involves the interfacial resistances of both electrodes. The equivalent circuit model used to fit the Nyquist plots is shown in **Figure 3-10**. The high-frequency real-axis intercept of the Nyquist plot corresponds to the resistance for ion conduction in the bulk electrolyte ( $R_{\text{bulk}}$ ). The Li/LiCoO<sub>2</sub> cell with the [Li(SL)<sub>2</sub>][TFSA] gel shows three depressed semicircles (**Figure 3-8a**, top). The EIS of the Li/Li symmetric cell was carried out to assess the impedance of the Li metal anode (**Figure 3-8a**, bottom). The Li/Li cell shows a semicircle in the frequency range of 10 kHz–100 Hz. This result suggests that the intermediate-frequency semicircle (10 kHz–100 Hz) of the Li/LiCoO<sub>2</sub> cell is mainly due to the charge transfer process at the Li metal anode ( $R_{\text{MF}}$ ). In fact, the intermediate-frequency semicircle hardly changed when the cell voltage is changed, because the electrode potential of the Li metal remains unchanged.

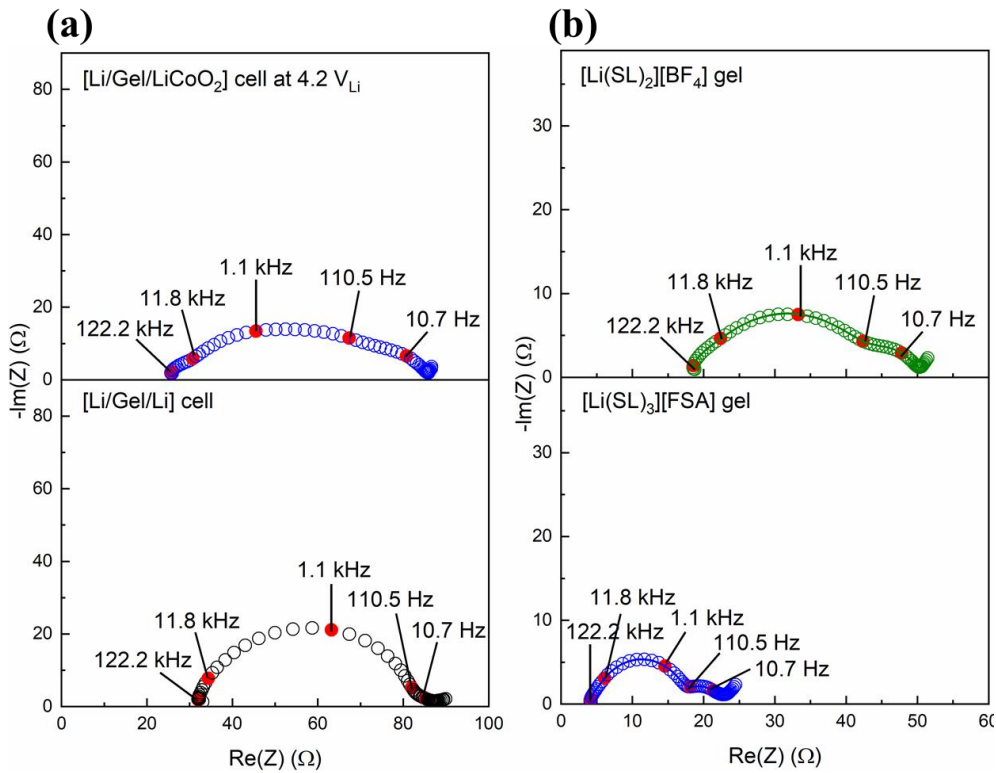


**Figure 3-8.** Nyquist plots of [Li(SL)<sub>2</sub>][TFSA] gel with different cell configuration of a symmetric cell of [Li/Gel/Li] or a half cell of [Li/Gel/LiCoO<sub>2</sub>] at 4.2 V<sub>Li</sub>. (b) Stacked Nyquist plots of a half cell of [Li/Gel/LiCoO<sub>2</sub>] gel electrolytes with various containing highly concentrated electrolytes at 30 °C. The cells were charged up to 4.2 V<sub>Li</sub> and the solid line represents the fitting line according to the equivalent circuit.

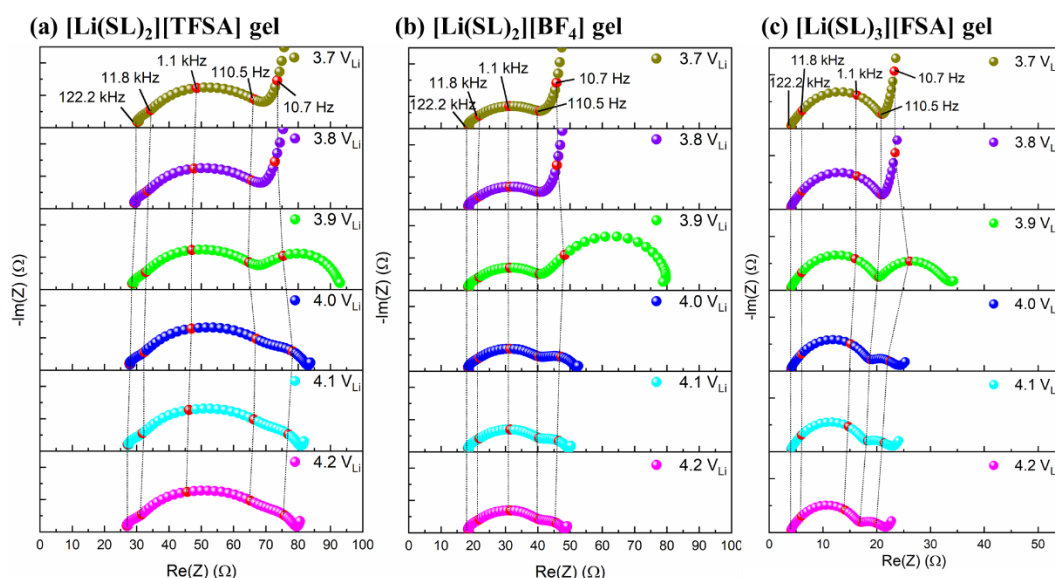


**Figure 3-9.** Stacked Nyquist plots of a [Li/Gel/LiCoO<sub>2</sub>] half cell with charge process of electrochemical potential range from 3.7 to 4.2 V<sub>Li</sub>.

However, unlike the intermediate-frequency semicircle, the low-frequency semicircle (100–1 Hz) shows potential dependence (**Figures 3-9**); it emerges at  $>3.9$  V<sub>Li</sub>, is accompanied by the redox reaction of LiCoO<sub>2</sub>, and becomes smaller when the voltage is further increased from 3.9 to 4.2 V<sub>Li</sub>. Therefore, the low-frequency semicircle can be assigned to the charge transfer process associated with Li-ion insertion/extraction at the LiCoO<sub>2</sub> cathode ( $R_{LF}$ ). The very small semicircle observed for the Li/LiCoO<sub>2</sub> cell in the high-frequency region ( $>10$  kHz), which is independent of the cell voltage (**Figure 3-10**), is assumed to be the impedance originating from ion migration and electron conduction processes in the porous LiCoO<sub>2</sub> cathode ( $R_{HF}$ ).<sup>30,31</sup> The Nyquist plots of the Li/LiCoO<sub>2</sub> cells were analyzed based on the equivalent circuit depicted in **Figure 3-10**; the obtained parameters,  $R_{bulk}$ ,  $R_{HF}$ ,  $R_{MF}$ , and  $R_{LF}$ , are listed in **Table 3-11**. Both the interfacial resistances of the Li metal anode ( $R_{MF}$ ) and LiCoO<sub>2</sub> cathode ( $R_{LF}$ ) are in the order of [Li(SL)<sub>2</sub>][TFSA]  $>$  [Li(SL)<sub>2</sub>][BF<sub>4</sub>]  $>$  [Li(SL)<sub>3</sub>][FSA]. The [Li(SL)<sub>3</sub>][FSA] gel electrolyte allows much faster charge transfer kinetics at the electrode/electrolyte

interfaces, which also contributes to the higher rate capability of the Li/LiCoO<sub>2</sub> cell.

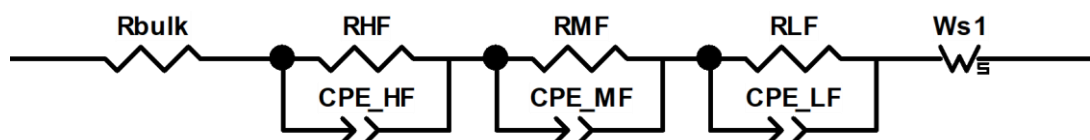


**Figure 3-10.** Equivalent circuit model of the [Li/Gel/LiCoO<sub>2</sub>] cell.

**Table 3-11.** The fitting values of the [Li/Gel/LiCoO<sub>2</sub>] cell.

	Thickness [ $\mu\text{m}$ ]	$R_{bulk}$ [ $\Omega$ ]	$R_{HF}$ [ $\Omega$ ]	$R_{LF}$ [ $\Omega$ ]	$R_{interface}$ [ $\Omega$ ]	$R_{total}$ [ $\Omega$ ]
[Li(SL) <sub>2</sub> ][TFSA]	48	22.61	46.65	10.42	57.07	79.68
[Li(SL) <sub>2</sub> ][BF <sub>4</sub> ]	50	17.73	25.82	6.65	32.47	50.20
[Li(SL) <sub>3</sub> ][FSA]	50	3.99	13.36	4.72	18.08	22.07

The  $R_{interface}$  is the sum of  $R_{HF}$  and  $R_{LF}$ . The values of  $R_{interface}$  increased in the order of [Li(SL)<sub>2</sub>][TFSA] > [Li(SL)<sub>3</sub>][BF<sub>4</sub>] > [Li(SL)<sub>3</sub>][FSA], which means slow kinetics for charge transfer reaction at the electrode/electrolyte interface (**Table 3-11**).

### 3.2.3 Voltage drop in the discharge curves

The initial voltage drop would be attributable to both ohmic resistance in the bulk electrolyte and the interfacial resistances at the electrode/electrolyte interfaces.

As can be seen in **Figures 3-5** and **3-6**, the cell voltage immediately drops once the discharge begins, and then gradually decreases further in the middle and end of the discharge process. The initial voltage drops, attributed to the total resistance  $R_{total}$  ( $= R_{bulk} + R_{HF} + R_{MF} + R_{LF}$ ) of the Li/LiCoO<sub>2</sub> cell, in the discharge curves of the Li/LiCoO<sub>2</sub> cells with the SL-based gel electrolytes are plotted in **Figure 3-12**

as a function of the discharge current. The initial voltage drop is roughly proportional to the discharge current,  $I$ , and the estimated voltage drop,  $I \times R_{\text{total}}$ , agrees well with the experimental value, especially in the lower-current region.<sup>32,33</sup> Upon discharge at high current, a Li salt concentration gradient forms in the gel electrolyte, which affects the discharge voltage profile. The decrease in the Li salt concentration at the cathode during a high-rate discharge decreases the electrode potential of LiCoO<sub>2</sub>. Conversely, the increase in the Li salt concentration at the anode surface elevates the electrode potential of the Li metal. This concentration polarization increases as the difference in the Li salt concentration between the anode and the cathode increases. During the discharge at high current, the concentration difference increases with time owing to the release and consumption of Li<sup>+</sup> at the anode and the cathode, respectively; therefore, the polarization becomes larger in the middle and end of the discharge. The concentration polarization could also be more efficiently suppressed with the [Li(SL)<sub>3</sub>][FSA] gel electrolyte owing to the fast Li-ion flux based on the high Li-ion conductivity (Table 3-4).

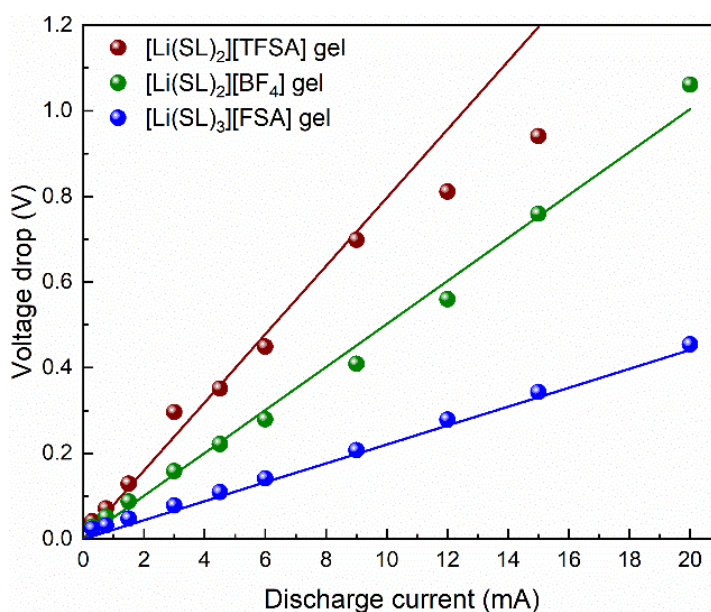


**Figure 3-12.** Nyquist plots of [Li(SL)<sub>2</sub>][TFSA] gel with different cell

configuration of a symmetric cell of [Li/Gel/Li] or a half cell of [Li/Gel/LiCoO<sub>2</sub>] at 4.2 V<sub>Li</sub>. Each solid line represents the calculated voltage drop based on the resistivities derived from **Table 3-11**.

### 3.3 Conclusions

In this work, highly Li-ion conductive gel electrolytes comprising PVDF–HFP and highly concentrated SL-based electrolytes were prepared using a solution casting method. The prepared SL-based gel electrolytes exhibited sufficient Li-ion conducting properties that can be applied to lithium secondary batteries. The highest Li-ion conductivity of  $3.8 \times 10^{-4} \text{ S cm}^{-1}$  and the lowest interfacial resistance achieved for [Li(SL)<sub>3</sub>][FSA] gel electrolyte contributed to the higher rate capability of the Li/LiCoO<sub>2</sub> cell than that of the cells with [Li(G4)][TFSA], [Li(SL)<sub>2</sub>][TFSA], and [Li(SL)<sub>2</sub>][BF<sub>4</sub>] gel electrolytes. The [Li(SL)<sub>3</sub>][FSA] gel demonstrated a high discharge capacity (98 mA h g<sup>-1</sup>) and coulombic efficiency (99.5%) at a high current density of 13.3 mA cm<sup>-2</sup>. It is indicated the importance of Li ion conductivity and fast charge transfer rate at the electrode/electrolyte interface, especially under high discharge current density where Li ions were involved in the rapid electrochemical reaction at the electrode/electrolyte interface. The results demonstrated that Li ion transport properties of gel electrolytes contribute in the Li/LiCoO<sub>2</sub> batteries.

### 3.4 References

- 1 B. Nykvist and M. Nilsson, 2015, **5**, 329–332.
- 2 A. Opitz, P. Badami, L. Shen, K. Vignarooban and A. M. Kannan, *Renew. Sustain. Energy Rev.*, 2017, **68**, 685–692.
- 3 N. Nitta, F. Wu, J. T. Lee and G. Yushin, *Mater. Today*, 2015, **18**, 252–264.
- 4 Y. Kato, S. Hori, T. Saito, K. Suzuki, M. Hirayama, A. Mitsui, M. Yonemura, H. Iba and R. Kanno, *Nat. Energy*, 2016, **1**, 1–7.
- 5 G. E. Blomgren, *J. Electrochem. Soc.*, 2017, **164**, A5019–A5025.

- 6 Y. Tian, G. Zeng, A. Rutt, T. Shi, H. Kim, J. Wang, J. Koettgen, Y. Sun, B. Ouyang, T. Chen, Z. Lun, Z. Rong, K. Persson and G. Ceder, *Chem. Rev.*, 2021, **121**, 1623–1669.
- 7 J. P. Zheng and T. R. Jow, *J. Power Sources*, 1996, **62**, 155–159.
- 8 B. G. Pollet, I. Staffell and J. L. Shang, *Electrochim. Acta*, 2012, **84**, 235–249.
- 9 M. Armand, *Nature*, 2001, **414**, 359–367.
- 10 P. Yang and J. Tarascon, *Nat. Mater.*, 2012, **11**, 560–563.
- 11 T. R. Jow, S. A. Delp, J. L. Allen, J. Jones and M. C. Smart, *J. Electrochem. Soc.*, 2018, **165**, 361–367.
- 12 F. Sagane, T. Abe and Z. Ogumi, *J. Electrochem. Soc.*, 2012, **159**, A1766–A1769.
- 13 Y. Yamada, Y. Iriyama, T. Abe and Z. Ogumi, *Langmuir*, 2009, **25**, 12766–12770.
- 14 Y. Yamada, F. Sagane, Y. Iriyama, T. Abe and Z. Ogumi, *J. Phys. Chem. C*, 2009, **113**, 14528–14532.
- 15 I. Yamada, K. Miyazaki, T. Fukutsuka, Y. Iriyama and T. Abe, *J. Power*, 2015, **294**, 460–464.
- 16 T. Minato and T. Abe, *Prog. Surf. Sci.*, 2017, **92**, 240–280.
- 17 C. Wang, K. Aoyagi, M. Aykol and T. Mueller, *ACS Appl. Mater. Interfaces*, 2020, **12**, 55510–55519.
- 18 M. Gauthier, T. J. Carney, A. Grimaud, L. Giordano, N. Pour, H. Chang, D. P. Fenning, S. F. Lux, O. Paschos, C. Bauer, F. Maglia, S. Lupart, P. Lamp and Y. Shao-horn, *J. Phys. Chem. Lett.*, 2015, **6**, 4653–4672.
- 19 M. D. Levi, G. Salitra, B. Markovsky, H. Teller, D. Aurbach, U. Heider and L. Heider, *J. Electrochem. Soc.*, 1999, **146**, 1279–1289.
- 20 R. N. Nasara, W. Ma, Y. Kondo, K. Miyazaki, Y. Miyahara, T. Fukutsuka, C. Lin, S. Lin and T. Abe, *ChemSusChem*, 2020, **13**, 4041–4050.
- 21 K. M. Diederichsen, E. J. Mcshane and B. D. Mccloskey, *ACS Energy Lett.*, 2017, **2**, 2563–2575.
- 22 J. Evans, C. A. Vincent and P. G. Bruce, *Polymer*, 1987, **28**, 2324–2328.
- 23 M. D. Galluzzo, J. A. Maslyn, D. B. Shah and N. P. Balsara, *J. Chem. Phys.*, , DOI:10.1063/1.5109684.
- 24 K. Shigenobu, K. Dokko, M. Watanabe and K. Ueno, *Phys. Chem. Chem. Phys.*, 2020, 15214–15221.
- 25 D. Dong, F. Salzer, B. Roling and D. Bedrov, *Phys. Chem. Chem. Phys.*, 2018, **20**, 29174–29183.
- 26 F. Wohde, M. Balabajew and B. Roling, *J. Electrochem. Soc.*, 2016, **163**, 714–721.
- 27 K. Dokko, D. Watanabe, Y. Ugata, M. L. Thomas, S. Tsuzuki, W. Shinoda, K. Hashimoto, K. Ueno, Y. Umebayashi and M. Watanabe, *J. Phys. Chem. B*, 2018, **122**, 10736–10745.

- 28 A. Nakanishi, K. Ueno, D. Watanabe, Y. Ugata, Y. Matsumae, J. Liu, M. L. Thomas, K. Dokko and M. Watanabe, *J. Phys. Chem. C*, 2019, **123**, 14229–14238.
- 29 T. Evans, J. Olson, V. Bhat and S. Lee, *J. Power Sources*, 2014, **269**, 616–620.
- 30 R. Tatara, P. Karayaylali, Y. Yu, Y. Zhang, L. Giordano, F. Maglia, R. Jung, J. P. Schmidt, I. Lund and Y. Shao-Horn, *J. Electrochem. Soc.*, 2019, **166**, 5090–5098.
- 31 A. Ikezawa, G. Fukunishi, T. Okajima, F. Kitamura, K. Suzuki, M. Hirayama, R. Kanno and H. Arai, *Electrochem. commun.*, 2020, **116**, 106743.
- 32 S. Piller, M. Perrin and A. Jossen, *J. Power Sources*, 2001, **96**, 113–120.
- 33 P. P. Prosini, *J. Electrochem. Soc.*, 2005, **152**, A1925–A1929.

## **Chapter Four**

Preparation of composite electrolytes composed of  
 $\text{Li}_{1.5}\text{Al}_{0.5}\text{Ti}_{1.5}(\text{PO}_4)_3$  and PVDF–HFP gel electrolytes containing  
high concentration Li salts

Part of the work presented in this chapter has been published as: J. Ock, M. Fujishiro, K. Ueno, I. Kawamura, R. Tatara, K. Hashimoto, M. Watanabe, and K. Dokko, *ACS Omega*, 2021, 6, 16187–16193.

In recent years, many attempts have been made to synthesize the composite electrolytes combining inorganic solid electrolytes with polymer electrolytes to achieve the synergistic effect.<sup>1–18</sup> Among polymer electrolytes, PEO-based polymer electrolytes are often used to fabricate SE–polymer composite electrolyte sheets. PEO exhibits excellent characteristics such as processability, flexibility, and Li<sup>+</sup> ion solvating properties.<sup>19–22</sup> However, PEO-based polymer electrolytes have relatively low ionic conductivity, in the order of 10<sup>-5</sup> S cm<sup>-1</sup> at room temperature, a low Li-ion transference number ( $t_+$ ) of ~0.2, and low oxidative stability (<4 V). Low  $t_+$  causes concentration polarization when a relatively high current density is applied to the polymer electrolyte, which limits the rate capability of the Li polymer batteries. PVDF-HFP based polymer gel electrolytes has been considered as another option of flexible solid electrolytes.<sup>23,24</sup> PVDF-HFP-based gel electrolytes containing an organic liquid electrolyte exhibit ionic conductivity in the order of ~10<sup>-3</sup> S cm<sup>-1</sup> and high electrochemical stability derived from the liquid electrolyte while a low Li-ion transference number in the gel electrolytes still poses a challenge.

In this chapter, composite electrolyte membranes comprising an SE, Li<sub>1.5</sub>Al<sub>0.5</sub>Ti<sub>1.5</sub>(PO<sub>4</sub>)<sub>3</sub> (LATP), and a gel electrolyte were fabricated. PVDF–HFP exhibits a relatively good mechanical strength and is electrochemically stable against both reduction and oxidation. This polymer can also support a relatively large amount (~80 wt.%) of liquid electrolyte in the matrix. In chapter 3, it is previously reported that PVDF–HFP gel electrolytes contained sulfolane-based highly concentrated electrolytes exhibit high  $t_+$  (0.6–0.8) and that Li batteries can be operated at a current density of ~13.3 mA cm<sup>-2</sup>, regardless of the relatively low ionic conductivity (0.2–0.7 mS cm<sup>-1</sup>) at room temperature. In this work, the

mechanical properties and Li<sup>+</sup> transport properties of the composite electrolyte membranes were investigated.

## 4.1 Synthesis of LATP inorganic electrolyte and composite electrolyte

In general, NASICON-type Li ion conductors are stable with air and moisture and could be operated at high potentials.<sup>25,26</sup> Among NASICON-type Li ion conductors, LATP has the highest ionic conductivity at room temperature that has been reported previously. In LATP, there is two  $[\text{TiO}_6]$  octahedra are linked to three  $[\text{PO}_4]$  tetrahedra by shared oxygens. The general symmetry of crystal framework is rhombohedral, thus, there are two sites for Li cations; M1 sites surrounded by six oxygen atoms and located at inversion centers and M3 sites surrounded by ten oxygen atoms and disposed symmetrically around ternary axes. Li ion hopping occurs through these Li sites (**Figure 4-1**).<sup>27,28</sup>

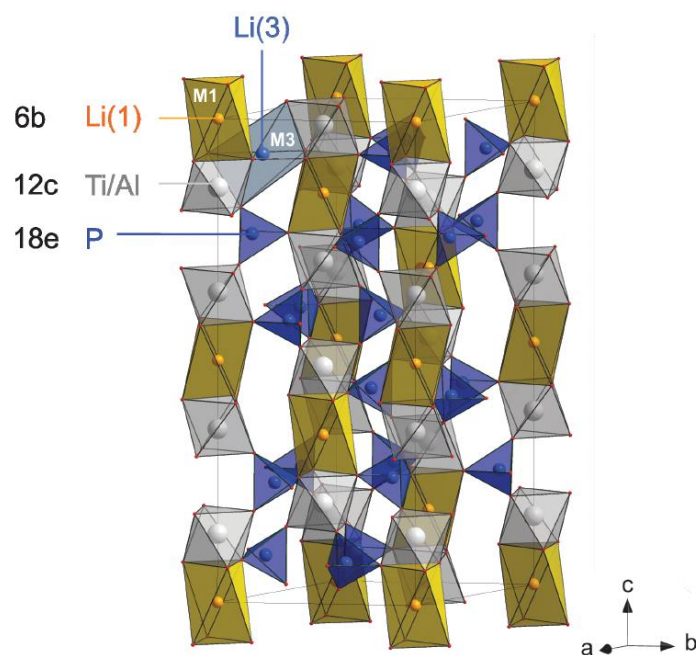


**Figure 4-1.** Crystal structure of  $\text{Li}_{0.5}\text{Al}_{1.5}\text{Ti}_{0.5}(\text{PO}_4)_3$ . Adopted from ref. 27 with permission from the Royal Society of Chemistry.

### 4.1.1 Materials and experiments

**Synthesis of  $\text{Li}_{1.5}\text{Al}_{0.5}\text{Ti}_{1.5}(\text{PO}_4)_3$  (LATP).** Precursors were used as received and the making process was reported in elsewhere.<sup>29,30</sup> The molar ratio of each precursors was prepared as follows.  $(\text{CH}_3\text{COOLi} : \text{Al}(\text{OC}_4\text{H}_9)_3 : \text{Ti}(\text{OC}_4\text{H}_9)_4 : \text{NH}_4\text{H}_2\text{PO}_4 : n\text{-C}_4\text{H}_9\text{OH}:\text{H}_2\text{O} = 1.5 : 0.5 : 1.5 : 3 : 50 : 800)$ .  $\text{Al}(\text{OC}_4\text{H}_9)_3$  (97%, Sigma-Aldrich) and  $\text{Ti}(\text{OC}_4\text{H}_9)_4$  (97%, Sigma-Aldrich) were dissolved into *n*- $\text{C}_4\text{H}_9\text{OH}$  (99%, Sigma-Aldrich). Then,  $\text{CH}_3\text{COOLi}$  (98%, Sigma-Aldrich) and  $\text{NH}_4\text{H}_2\text{PO}_4$  (99%, Sigma-Aldrich) were dissolved into purified  $\text{H}_2\text{O}$ . Two solutions were homogeneously mixed at 60 °C for 2 h to prepare the Li-Al-Ti-( $\text{PO}_4$ ) sol. The prepared sol was dried at 100 °C, then dried powder was calcined at 500 °C for 4 h in air to obtain amorphous LATP powder. The grounded powder was directly transferred into alumina boat or uniaxial pressurized in a 13 mm diameter die at 350 MPa, followed by calcination at 950 °C for 12h. Calcined pellet was gold sputtered both sides with ion sputter (E-1010, Hitachi).

As-synthesized LATP contained a small amount of  $\text{AlPO}_4$  as impurity (**Figure 4-2**), possibly derived from the thermal decomposition of LATP during calcination at high temperatures.<sup>28,31</sup>

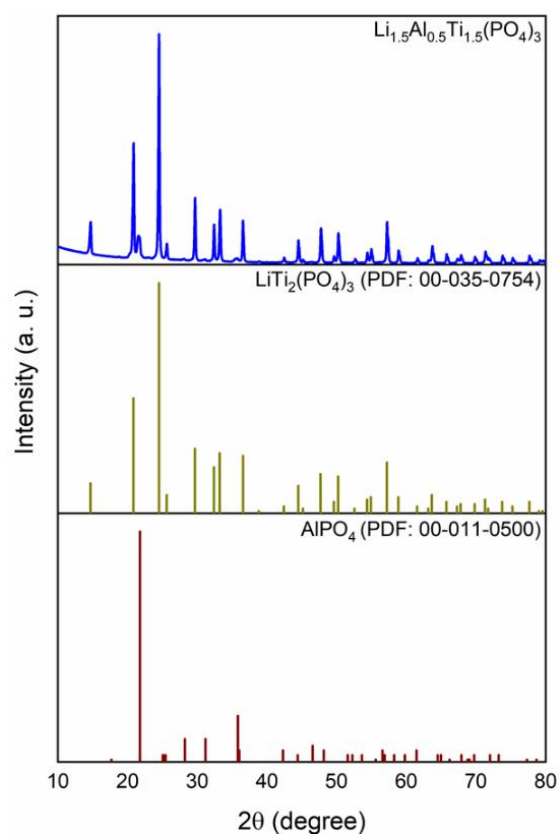


**Figure 4-2.** XRD patterns of synthesized LATP particles.

## 4.2 Morphologies and mechanical properties of composite electrolytes

**Tensile test.** The membranes were cut into dumbbell shape and tensile properties were measured using a Shimadzu EZ-LX at a cross-head speed of  $10 \text{ mm min}^{-1}$ . The Young's modulus and fracture energy of the composite electrolytes were evaluated from the slope of the stress-strain curve (0.03 – 0.08 N) and the area in stress-strain curves, respectively.

**FE-SEM measurements.** The morphology of composite electrolytes was characterized using field emission scanning electron microscopy (FE-SEM, SU

8010, Hitachi). FE-SEM images of Au sputtered  $\text{Li}_{1.5}\text{Al}_{0.5}\text{Ti}_{1.5}(\text{PO}_4)_3$  (LATP) pellet with cross sectional plane polished by focus ion beam scanning electron microscopes (FIB-SEM, JIB-4501, JEOL). Surface milling was conducted using Ga ions (10 to 5 kV).

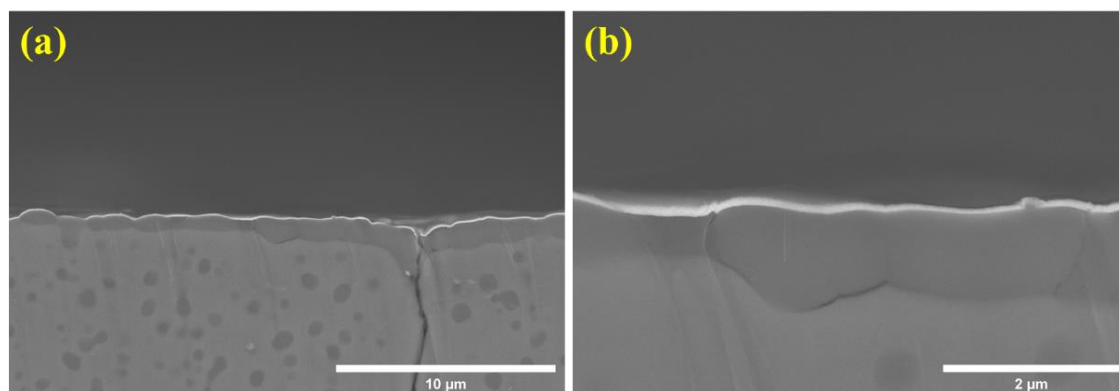


**Figure 4-3.** FE-SEM images of Au sputtered LATP pellet polished by cross section polisher (JEOL IB-09010CP). The average thickness of sputtered Au layer on the LATP pellet was found to be 100 nm.

#### 4.2.1 Morphologies of composite electrolyte

**Figure 4-4** shows the FE-SEM images of the LATP samples. The diameter of synthesized LATP powder was around micrometer scale (**Figure 4-4a**). A FE-SEM image of LATP pellet with cross sectional plane polished by FIB-SEM is shown in **Figure 4-4(b-d)**. It showed lots of pores and cracks throughout the pellet, which may cause unneeded interrupt of the Li ion transport in the bulk electrolyte and result in a large resistance in the cell.

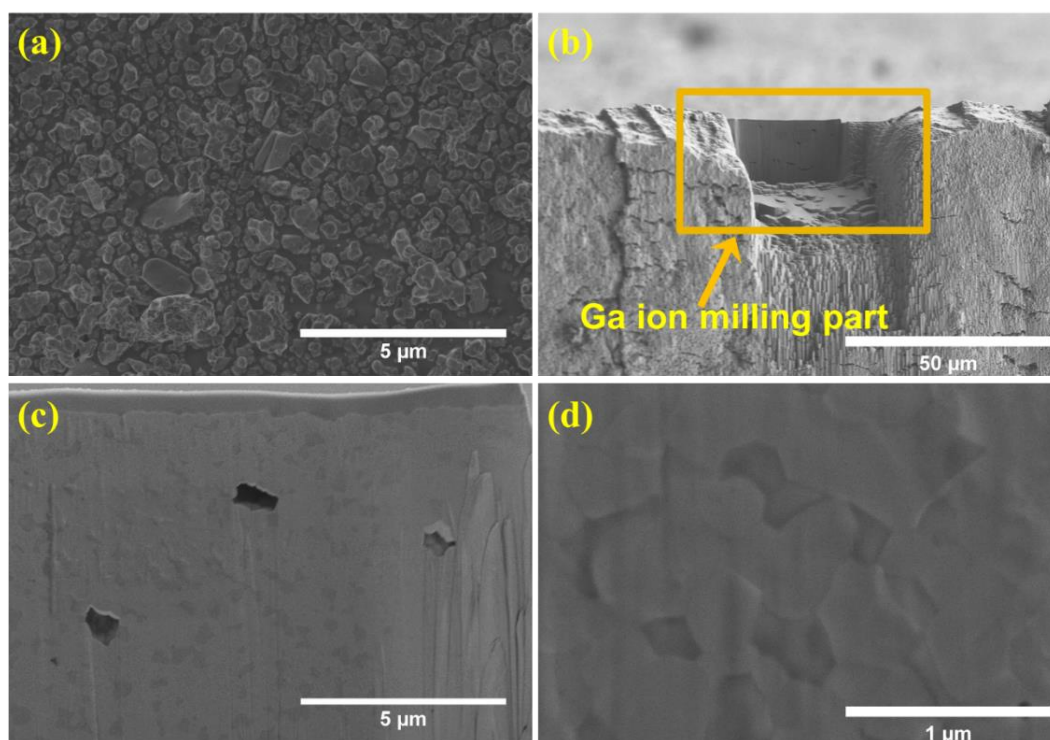


**Figure 4-4.** FE-SEM images of LATP pellet with heat treatment at 950 °C for 12 h of (a) LATP powder and (b-d) cross sectional plane of LATP pellet polished by FIB-SEM.

**Figure 4-5** shows the FE-SEM images of the composite electrolytes. For the Gel100 membrane (without LATP), no pores can be observed over the surface, indicating that the membrane was uniformly formed during the evaporation of the casting solvent.<sup>23</sup> However, small pores can be observed in Gel70-LATP30 (**Figure 4-5b**) and Gel40-LATP60 (**Figure 4-5c**). The pores might have been created during the evaporation of the solvent (acetone) between the LATP particles.

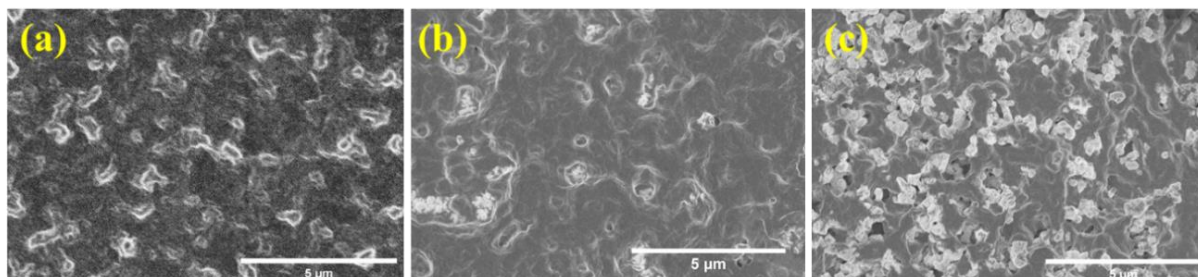


**Figure 4-5.** FE-SEM images of composite electrolytes of (a) Gel 100, (b) Gel70-LATP30 and (c) Gel40-LATP60.

## 4.2.2 Results of tensile measurements

Tensile tests were performed to evaluate the mechanical strength of the membranes. **Figure 4-6** shows the stress–strain curves of the composite membranes, and the mechanical properties are summarized in **Table 4-7**. Gel100 showed deformation properties, and the fracture strain was 224% with a tensile strength of 2.67 MPa. With an increase in the amount of LATP, the fracture strain gradually decreased. It is worth mentioning that even at a high content of LATP (Gel40-LATP60), the composite electrolyte remained flexible, as shown in **Figure 4b**.

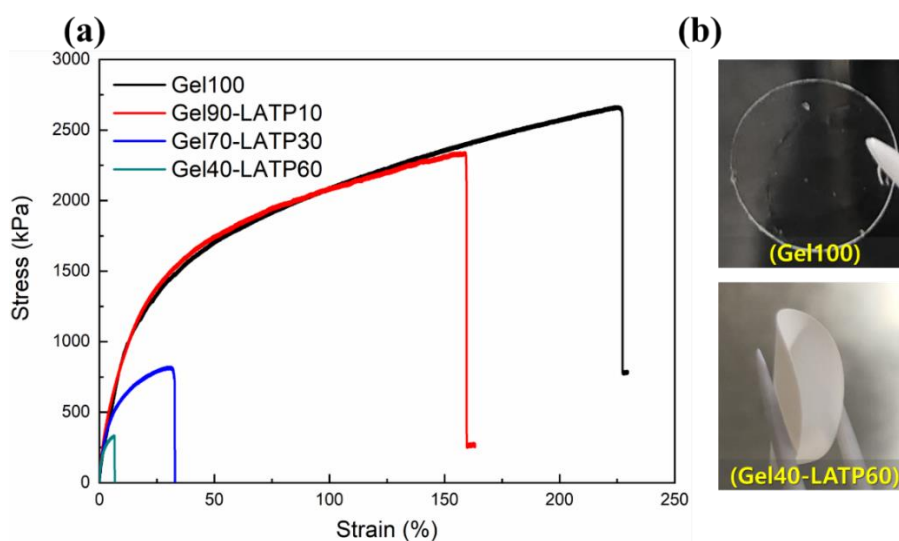


**Figure 4-6.** Stress–strain curves of the composite electrolytes with different LATP compositions measured at room temperature. (b) Images of Gel100 and Gel40-LATP60 membranes.

**Table 4-7.** Young’s modulus, tensile strength, fracture strain, and fracture energy of composite electrolytes with different amounts of LATP particles.

[Gel]-[LATP] / Weight %	pvdF-co-hfp / Weight %	Young’s modulus / Mpa (0.03–0.08 N)	Tensile strength / Mpa	Fracture strain / %	Fracture energy / kJ m <sup>-3</sup>
Gel100	30	8.78	2.67	224	4528
Gel90-LATP10	27	10.44	2.34	159	2886
Gel70-LATP30	21	10.27	0.82	30	188
Gel40-LATP60	12	7.06	0.34	6	16

### 4.3 Li ion exchange of composite electrolyte

Li ions preferred pathway in the composite could be identified by performing <sup>6</sup>Li/<sup>7</sup>Li isotope exchange experiment.<sup>32–35</sup> Based on the natural abundance of the <sup>6</sup>Li (7.6%) ion, Li ion pathway in the composites can be traced by quantitatively identifying the <sup>6</sup>Li peak from each component with <sup>6</sup>Li MAS-NMR. Li ion exchange reaction through the [<sup>6</sup>Li(SL)<sub>2</sub>][TFSA] | LATP interface was investigated by simply mixing the [<sup>6</sup>Li(SL)<sub>2</sub>][TFSA] and LATP powder, which provided insight of the intrinsic Li ion exchange behavior at the interface. Additionally, under biased applied potential with <sup>6</sup>Li symmetric cells, the <sup>7</sup>Li ions in the composites were partially replaced with the <sup>6</sup>Li ions and consequently we could trace the Li ion pathway within the composite electrolytes.

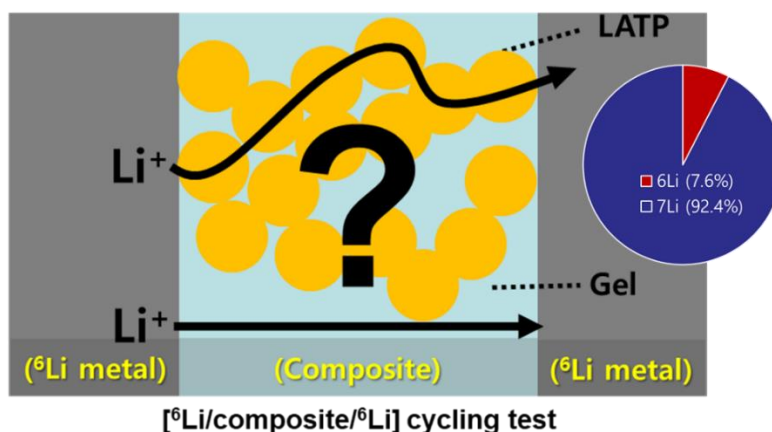


**Figure 4-8.** Schematic image of  ${}^6\text{Li}$  (7.6%)  $\rightarrow$   ${}^7\text{Li}$  (92.4%) isotope exchanged from the  ${}^6\text{Li}$  symmetric cells.

### 4.3.1 Materials and experiments

$[{}^6\text{Li}(\text{SL})_2][\text{TFSA}] \mid \text{LATP}$ .

${}^6\text{LiN}(\text{SO}_2\text{CF}_3)_2$  ( $\text{LiTFSA}$ ) was synthesized by neutralization of  $\text{HN}(\text{SO}_2\text{CF}_3)_2$  ( $\text{HTFSA}$ , 99%, Kanto Chemical) and  ${}^6\text{Li}_2\text{CO}_3$  (95%, Sigma-Aldrich).  ${}^6\text{Li}_2\text{CO}_3$  was mixed with  $\text{HTFSA}$  in a 1:2 molar ratio in water and stirred overnight. After neutralization, the water was evaporated using a rotary evaporator to obtain  ${}^6\text{LiTFSA}$ .  ${}^6\text{LiTFSA}$  was further dried under vacuum at 120 °C for over 24 h. The obtained  ${}^6\text{LiTFSA}$  was stored in an Ar-filled glove box ( $\text{VAC}$ ,  $[\text{H}_2\text{O}] < 0.5$  ppm). Sulfolane (SL) and  ${}^6\text{LiTFSA}$  were mixed in a 2:1 molar ratio and stirred overnight at 60 °C to obtain a homogeneous liquid of  $[{}^6\text{Li}(\text{SL})_2][\text{TFSA}]$ .

The  $\text{Li}^+$  ion exchange between  $[{}^6\text{Li}(\text{SL})_2][\text{TFSA}]$  and LATP powder was examined. The LATP powder was immersed in  $[{}^6\text{Li}(\text{SL})_2][\text{TFSA}]$  and stirred at 30 °C for over 48 h. Subsequently, the LATP was washed with tetrahydrofuran (99%, Wako Chemical) several times to remove  $[{}^6\text{Li}(\text{SL})_2][\text{TFSA}]$ . The  $\text{Li}^+$ -exchanged LATP powder was dried under vacuum at 50 °C overnight and then transferred to a 4.0 mm o.d. zirconia-type NMR tube.

### **[<sup>6</sup>Li symmetric cell cycling test].**

<sup>6</sup>Li metal chunk (95 %, Sigma-Aldrich) was beaten out into thin sheet and punched into a circle (14 mm diameter). The 2032 coin cell type <sup>6</sup>Li symmetric cell was assembled in an Ar-filled glove box. The <sup>6</sup>Li symmetric cells were aged at 30 °C for a day and subsequently cycling measurements were carried out using at a constant current density of 15 μA cm<sup>-2</sup> for about a dozen times. The [Li(SL)<sub>2</sub>][TFSA] gel was used as buffer layer in an effort to avoid the reduction reaction between transition metal ion (Ti<sup>4+</sup>) and Li metal, which has been reported elsewhere. After cycling tests, the <sup>6</sup>Li cycled coin cell of each composition was disassembled in an Ar-filled glove box and transferred into the NMR tubes.

Solid-state <sup>6</sup>Li magic-angle spinning (MAS) NMR measurements were performed on a Bruker 600 MHz AVANCE NMR spectrometer operated at a <sup>6</sup>Li resonance frequency of 88.31 MHz. <sup>6</sup>Li NMR spectra using a 90° excitation pulse of 3.6 μs and a repetition time of 100 s were acquired at an MAS frequency of 13 kHz at room temperature. The <sup>6</sup>Li chemical shift was externally referenced to 1 M LiCl aqueous solution at 0.0 ppm.

### **4.3.2 Li ion exchange of composite electrolyte**

To examine whether Li<sup>+</sup> ion exchange occurs, we simply mixed LATP powder and the liquid electrolyte of [<sup>6</sup>Li(SL)<sub>2</sub>][TFSA] for 48 h. Subsequently, solid-state <sup>6</sup>Li magic-angle spinning (MAS) NMR measurements were performed on the LATP powder. **Figure 4-9a** shows the <sup>6</sup>Li NMR spectra for the pristine LATP powder and the LATP powder treated with the liquid electrolyte of [<sup>6</sup>Li(SL)<sub>2</sub>][TFSA]. The <sup>6</sup>Li signal for the pristine LATP was observed at a chemical shift of -1.15 ppm, which is consistent with the reported value.<sup>36,37</sup> The intensity of the <sup>6</sup>Li signal was significantly increased after mixing with the [<sup>6</sup>Li(SL)<sub>2</sub>][TFSA] electrolyte,

suggesting that  $\text{Li}^+$  exchange occurred at the interface between LATP and  $[\text{Li}(\text{SL})_2][\text{TFSA}]$  and  ${}^6\text{Li}^+$  diffused into the bulk of the LATP particles.

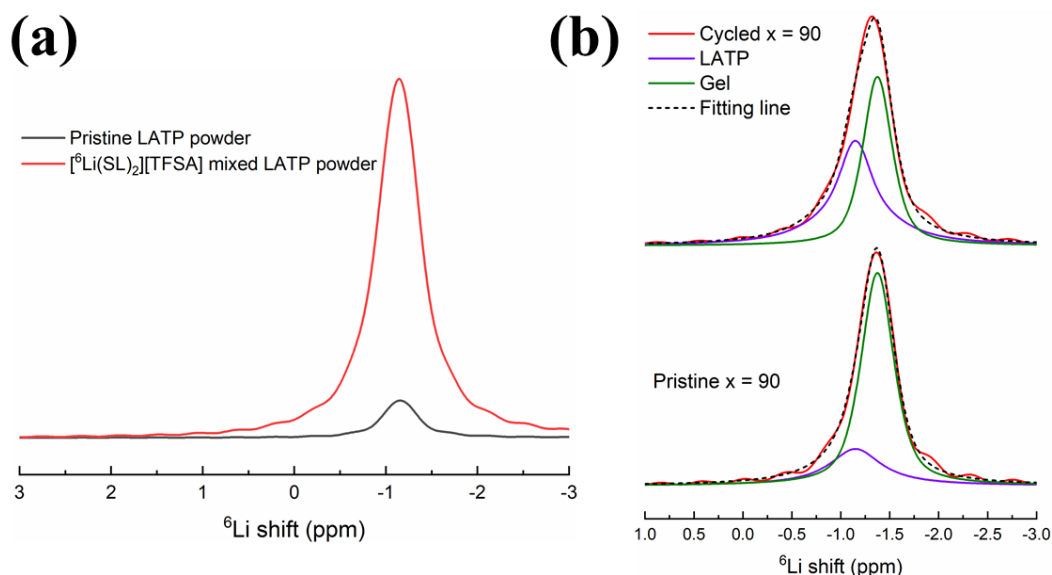


**Figure 4-9.**  ${}^6\text{Li}$  NMR peak comparison of (a) pristine LATP powder (black) and that mixed with  $[\text{Li}(\text{SL})_2][\text{TFSA}]$  at  $30\text{ }^\circ\text{C}$  for two days (red). (b) Deconvolution peaks of pristine/cycled Gel90-LATP10 composite electrolytes observed from MAS-NMR.

Additionally, composite electrolytes with different amounts of inorganic filler were measured by  ${}^6\text{Li}$  cycling test. Composite electrolyte was sandwiched between thin  $[\text{Li}(\text{SL})_2][\text{TFSA}]$  gel electrolyte to prevent the side reaction between  ${}^6\text{Li}$  metal and LATP particles, and the resulting Li stripping/plating behavior showed stable cell voltage at a relatively small overpotential of  $\sim 0.05\text{ V}$  (**Figure 4-10**). The pristine  ${}^6\text{Li}$  peaks of gel and Gel90-LATP10 ( $x = 90$ ) observed at around  $-1.375\text{ ppm}$  and  $-1.365\text{ ppm}$ , respectively (**Figure 4-9b**). In the case of composites, the observed peak could be deconvoluted into the center peak of each component. After  ${}^6\text{Li}$  cycling test of the ( $x = 90$ ) composite electrolyte, the  ${}^6\text{Li}$  chemical shift move from  $-1.365\text{ ppm}$  to  $-1.319\text{ ppm}$ , resulting in changing the volume fraction

of Li ion in LATP from 23 % to 38%, as observed in (**Figure 4-9b**). Based on the volumetric fraction of the LATP powder is around 5.9% in (**Table 4-11**), it is expected that gel matrix is mainly formed and LATP powder is sparsely dotted in the membrane. The increased relative amount of Li ion in LATP component after cycling, suggesting that Li ions exchange occurred at the gel/LATP interface.

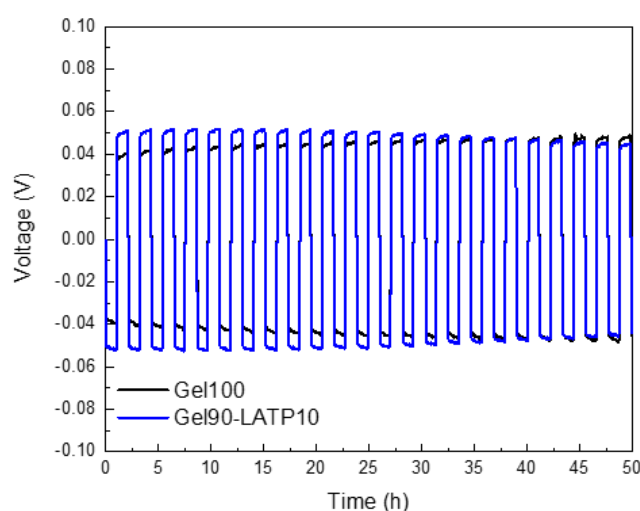


**Figure 4-10.** The voltage profiles of  ${}^6\text{Li} \rightarrow {}^7\text{Li}$  isotope exchange cycling test performed at  $15 \mu\text{A cm}^{-2}$ .

**Table 4-11.** The volume percent of composite electrolytes. The lithium mol percent can be calculated by using lithium concentration of LATP ( $11.42 \text{ mol L}^{-1}$ ) and  $[\text{Li}(\text{SL})_2][\text{TFSA}]$  ( $2.98 \text{ mol L}^{-1}$ ).<sup>11</sup>

<b>(Gel90-LATP10)</b>	LATP	$[\text{Li}(\text{SL})_2][\text{TFSA}]$	PVDF- <i>co</i> -HFP
Density ( $\text{g/cm}^3$ )	2.90	1.57	1.78
Weight (g)	0.10	0.63	0.27
Volume (%)	5.86	68.34	25.80
Li mol (%)	0.25	0.75	
Li % from MAS-NMR (Pristine ${}^6\text{Li}$ peak)	0.23	0.77	

## 4.4 Conclusions

In summary, a Li ion conductive solid electrolyte  $\text{Li}_{1.5}\text{Al}_{0.5}\text{Ti}_{1.5}(\text{PO}_4)_3$  (LATP) by a sol-gel process, which is stable with air and moisture and stable at high potentials as reported. The cross-sectional images of LATP pellet shows that cracks and pores were formed throughout the pellet, which is accounted as the reason of large interfacial resistance between electrode/electrolyte. Their mechanical and electrochemical properties could be improved by incorporating inorganic fillers into the polymer as reported. A flexible composite electrolyte was prepared by combining LATP fillers and the gel electrolyte of  $[\text{Li}(\text{SL})_2][\text{TFSA}]$  by a solution casting method. Local Li ions exchange environment have been investigated by 1D high-resolution (signal to noise ratio  $\approx 800$ )  $^6\text{Li}$  NMR, which was turned out to be Li ions exchanged at the interface between LATP and gel component. The pure gel shows remarkable stretchable property, and the fracture strain was 224 % with the tensile strength at 2.67 MPa. The Young's modulus of the composite electrolyte is independent of the LATP content, suggesting that the elastic property of the composite electrolyte is mainly due to the gel phase. Nevertheless, the composite electrolyte remained flexible even at a high content of LATP.

## 4.5 References

- 1 L. Fan, S. Wei, S. Li, Q. Li and Y. Lu, *Adv. Energy Mater.*, 2018, 8.
- 2 Y. Li, B. Xu, H. Xu, H. Duan, X. Lü, S. Xin, W. Zhou, L. Xue, G. Fu, A. Manthiram and J. B. Goodenough, *Angew. Chemie - Int. Ed.*, 2017, **56**, 753–756.
- 3 S. Kim, Y. Jung, D. Kim, W. Shin, M. Ue and D.-W. Kim, *J. Electrochem. Soc.*, 2016, **163**, 974–980.
- 4 T. Yuuki, Y. Konosu, M. Ashizawa, T. Iwahashi, Y. Ouchi, Y. Tominaga, R. Ooyabu, H. Matsumoto and H. Matsumoto, *ACS Omega*, 2017, **2**, 835–841.
- 5 Y. Shi, J. Zhang, A. M. Bruck, Y. Zhang, J. Li, E. A. Stach, K. J.

- Takeuchi, A. C. Marschilok, E. S. Takeuchi and G. Yu, *Adv. Mater.*, 2017, **29**, 1–8.
- 6 D. Li, Y. Wang and Y. Xia, *Nano Lett.*, 2003, **3**, 1167–1171.
- 7 C. W. Lin, C. L. Hung, M. Venkateswarlu and B. J. Hwang, *J. Power Sources*, 2005, **146**, 397–401.
- 8 F. Croce, G. B. Appetecchi, L. Persi and B. Scrosati, *Nature*, 1998, **394**, 456–458.
- 9 F. Croce, L. Persi, B. Scrosati, F. Serraino-fiory, E. Plichta and M. A. Hendrickson, *Electrochim. Acta*, 2001, **46**, 2457–2461.
- 10 X. Zhang, J. Xie, F. Shi, D. Lin, Y. Liu, W. Liu, A. Pei, Y. Gong, H. Wang, K. Liu, Y. Xiang and Y. Cui, *Nano Lett.*, 2018, **18**, 3829–3838.
- 11 M. Keller, A. Varzi and S. Passerini, *J. Power Sources*, 2018, **392**, 206–225.
- 12 A. M. Stephan and K. S. Nahm, *Polymer*, 2006, **47**, 5952–5964.
- 13 W. Liu, S. W. Lee, D. Lin, F. Shi, S. Wang, A. D. Sendek and Y. Cui, *Nat. Energy*, 2017, **17035**, 1–7.
- 14 N. Angulakshmi, D. J. Yoo, K. S. Nahm, C. Gerbaldi and A. M. Stephan, *Ionics*, 2014, **20**, 151–156.
- 15 M. Armand, *Polymer*, 1983, **9–10**, 745–754.
- 16 Z. Chen, P. A. Fitzgerald, G. G. Warr and R. Atkin, *Phys. Chem. Chem. Phys.*, 2015, **17**, 14872–14878.
- 17 N. M. Asl, J. Keith, C. Lim, L. Zhu and Y. Kim, *Electrochim. Acta*, 2012, **79**, 8–16.
- 18 L. Yang, Z. Wang, Y. Feng, R. Tan, Y. Zuo, R. Gao, Y. Zhao, L. Han, Z. Wang and F. Pan, *Adv. Energy Mater.*, 2017, **7**, 1701437.
- 19 J. W. Fergus, *J. Power Sources*, 2010, **195**, 4554–4569.
- 20 N. Wu, P. H. Chien, Y. Li, A. Dolocan, H. Xu, B. Xu, N. S. Grundish, H. Jin, Y. Y. Hu and J. B. Goodenough, *J. Am. Chem. Soc.*, 2020, **142**, 2497–2505.
- 21 W. Wang, E. Yi, A. J. Fici, R. M. Laine and J. Kieffer, *J. Phys. Chem. C*, 2017, **121**, 2563–2573.
- 22 X. Tao, Y. Liu, W. Liu, G. Zhou, J. Zhao, D. Lin, C. Zu, O. Sheng, W. Zhang, H. W. Lee and Y. Cui, *Nano Lett.*, 2017, **17**, 2967–2972.
- 23 T. Michot, A. Nishimoto and M. Watanabe, *Electrochim. Acta*, 2000, **45**, 1347–1360.
- 24 K. Elamin, M. Shojaatlohosseini, O. Danyliv, A. Martinelli and J. Swenson, *Electrochim. Acta*, 2019, **299**, 979–986.
- 25 A. Hayashi, N. Masuzawa, S. Yubuchi, F. Tsuji, C. Hotehama, A. Sakuda and M. Tatsumisago, *Nat. Commun.*, 2019, **10**, 1–6.
- 26 A. Martínez-Juárez, C. Pecharraoma, J. E. Iglesias and M. J. Rojo, *J. Phys. Chem. B*, 1998, **102**, 372–375.
- 27 V. Epp, Q. Ma, E. Hammer, F. Tietz and M. Wilkening, *Phys. Chem.*

- Chem. Phys.*, 2015, **17**, 32115–32121.
- 28 J. C. Bachman, S. Muiy, A. Grimaud, H. H. Chang, N. Pour, S. F. Lux, O. Paschos, F. Maglia, S. Lupart, P. Lamp, L. Giordano and Y. Shao-Horn, *Chem. Rev.*, 2016, **116**, 140–162.
- 29 Y. Isshiki, K. Dokko and K. Kanamura, *J.Jpn.Soc.Powder Powder Metall.*, 2006, **53**, 856–859.
- 30 H. Nakano, K. Dokko, M. Hara, Y. Isshiki and K. Kanamura, *Ionics*, 2008, **14**, 173–177.
- 31 L. Xingang, T. Jiang, J. Fu, R. Yuan, H. Wen and C. Zhang, *ACS Appl. Mater. Interfaces*, 2017, **9**, 11696–11703.
- 32 T. Yang, J. Zheng, Q. Cheng, Y. Y. Hu and C. K. Chan, *ACS Appl. Mater. Interfaces*, 2017, **9**, 21773–21780.
- 33 J. Zheng and Y. Y. Hu, *ACS Appl. Mater. Interfaces*, 2018, **10**, 4113–4120.
- 34 J. Zheng, H. Dang, X. Feng, P. H. Chien and Y. Y. Hu, *J. Mater. Chem. A*, 2017, **5**, 18457–18463.
- 35 J. Zheng, P. Wang, H. Liu and Y. Y. Hu, *ACS Appl. Energy Mater.*, 2019, **2**, 1452–1459.
- 36 K. Arbi, S. Mandal, J. M. Rojo and J. Sanz, *Chem. Mater.*, 2002, 1091–1097.
- 37 C. Vinod Chandran, S. Pristat, E. Witt, F. Tietz and P. Heitjans, *J. Phys. Chem. C*, 2016, **120**, 8436–8442.

## **Chapter Five**

Electrochemical properties of  $\text{Li}_{1.5}\text{Al}_{0.5}\text{Ti}_{1.5}(\text{PO}_4)_3/\text{PVDF-HFP}$  gel  
electrolyte

Part of the work presented in this chapter has been published as: J. Ock, M. Fujishiro, K. Ueno, I. Kawamura, R. Tatara, K. Hashimoto, M. Watanabe, and K. Dokko, *ACS Omega*, 2021, 6, 16187–16193

## 5.1 Rate performance of composite electrolytes

Li/LiCoO<sub>2</sub> cells were assembled with composite electrolytes (thickness: ca. 100 μm), and charge–discharge tests were conducted at 60 °C. **Figure 5-1** shows the discharge curves of the cells with Gel90-LATP10 and Gel40-LATP60 measured at various current densities. At a low current density of 0.2 mA cm<sup>-2</sup>, the cells exhibited discharge capacities in the range of 120–140 mA h g<sup>-1</sup>, which is close to the theoretical capacity (137 mA h g<sup>-1</sup>) of the redox reaction of LiCoO<sub>2</sub>/Li<sub>0.5</sub>CoO<sub>2</sub>.<sup>1</sup> LATP is known to react with Li metal, and the Ti<sup>4+</sup> in LATP is reduced to Ti<sup>3+</sup> through the reaction.<sup>2–6</sup> However, the Li/LiCoO<sub>2</sub> could be operated successfully with the composite electrolytes. Probably, the LATP particles in contact with Li metal were reduced, however, the reduction reaction of LATP did not propagate into the inside of the composite electrolytes due to the low electronic conductivity of LATP. In addition, the gel electrolyte between the LATP particles might inhibit the propagation of the reduction reaction. As shown in **Figure 5-1**, with increasing current density, the discharge voltage decreases because of the IR drop in the electrolyte membrane and the overvoltage for the electrochemical reactions in the cells. Apparently, the discharge voltage of the cell with Gel40-LATP60 was lower than that of the cell with Gel90-LATP10 at high current densities. In addition, the discharge capacity of the cell with Gel40-LATP60 was lower than that of the cell with Gel90-LATP10. The cells with Gel90-LATP10 and Gel40-LATP60 showed discharge capacities of 113 mAh g<sup>-1</sup> and 63 mAh g<sup>-1</sup>, respectively, at 4 mA cm<sup>-2</sup>. These results suggest that the internal resistance of the cell with Gel40-LATP60 was higher than that of the cell with Gel90-LATP10. Regardless of the Li<sup>+</sup>

exchange, the LATP particles hardly contribute to ionic conduction in the composite electrolyte. A possible hypothesis is the slow kinetics of  $\text{Li}^+$  ion exchange at the LATP/gel interface. If the interfacial Li-ion exchange is relatively slow, Li ions mainly migrate within the continuous gel phase and do not often pass through the LATP/gel interface in the composite electrolyte.

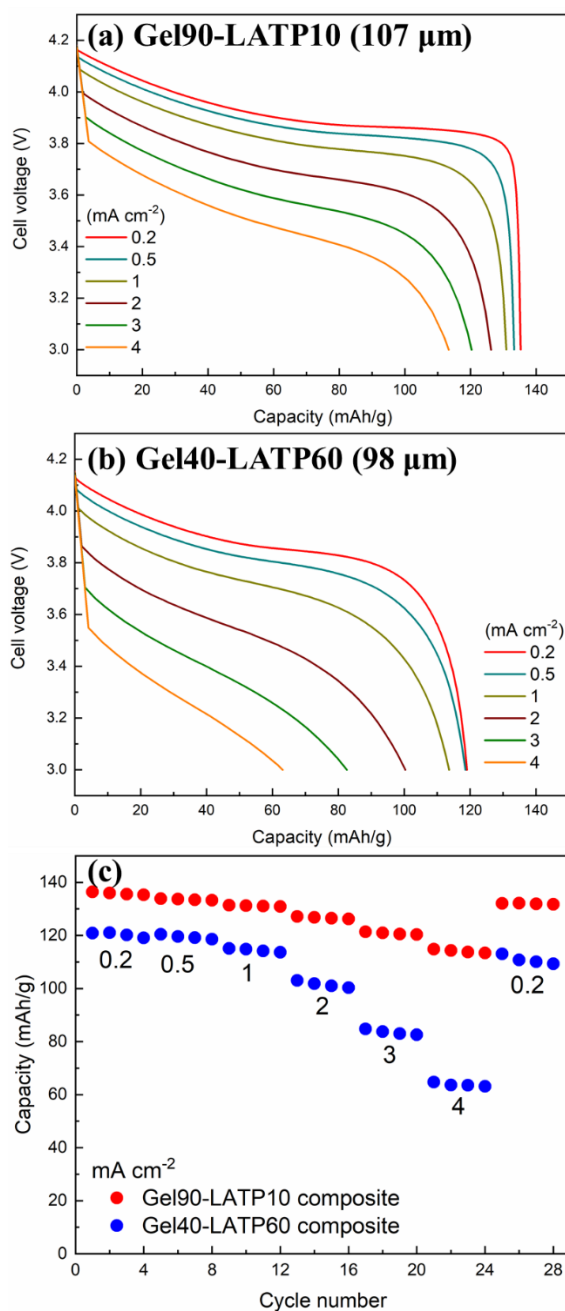


**Figure 5-1.** Discharge curves of [Li/composite electrolyte/LiCoO<sub>2</sub>] cells with (a) Gel90-LATP10 and (b) Gel40-LATP60 composite electrolytes measured at 60 °C. (c) Discharge capacities of the cells measured at various current densities. The cells were charged up to 4.2 V at a current density of 0.2 mA cm<sup>-2</sup> prior to each discharge.

## 5.2 Ionic conductivity of composite electrolytes

The ionic conductivity of the composite electrolyte was measured to determine the origin of the internal resistance of the cell. **Figure 5-2a** shows the ionic conductivity of the composite electrolytes with various LATP contents at 30 °C. The ionic conductivity of the composite electrolyte decreases with increasing LATP fraction and became as low as  $3.13 \times 10^{-6}$  S cm<sup>-1</sup> in Gel30-LATP70, which is lower than that of the LATP pellet ( $1.31 \times 10^{-5}$  S cm<sup>-1</sup>).<sup>7</sup> **Figure 5-2b** shows the Arrhenius plots of the conductivity of the electrolytes. Arrhenius plots of the conductivities of composite electrolytes showed convex-curved profiles, which are common behaviors of ionic conduction in organic electrolytes and can be expressed by Vogel–Fulcher–Tamman (VFT) equation. Apparently, the activation energy for ionic conduction in each composite electrolyte is similar to that of the gel electrolyte (without LATP). These suggest that ionic conduction mainly occurs in the gel phase. This indicates that the LATP particles in the composite electrolyte hardly contribute to ionic conduction. In the composite electrolytes, the LATP particles might be scarcely connected to each other and do not form a continuous phase. Indeed, the Young's modulus of the composite electrolyte is largely independent of the LATP content, suggesting that the elastic property of the composite electrolyte is mainly due to the gel phase. In other words, the gel forms a continuous phase in the composite electrolyte, and the LATP particles are dispersed in the gel matrix.

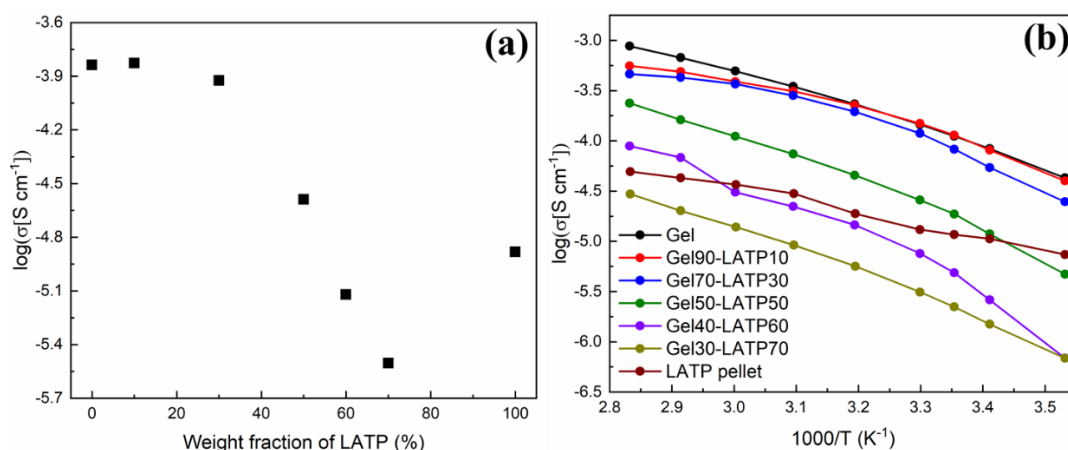


**Figure 5-2.** (a) Ionic conductivity of the composite electrolytes as a function of the LAMP content at 30 °C. (b) Arrhenius plots of the conductivity of composite electrolytes.

### 5.3 Interfacial resistance at the interface of LAMP and gel electrolyte

#### 5.3.1 Experiments

To clarify the interfacial resistance between gel and inorganic, we used sodium super ionic conductor (NASICON) type LiCGC plate ( $\text{Li}_2\text{O-Al}_2\text{O}_3\text{-SiO}_2\text{-P}_2\text{O}_5\text{-TiO}_2\text{-GeO}_2\text{-System}$ , Ohara corporation), where crystal structure and ionic conductivity is similar to the as-synthesized LAMP pellet, as non-porous inorganic model (**Figure 5-3**).

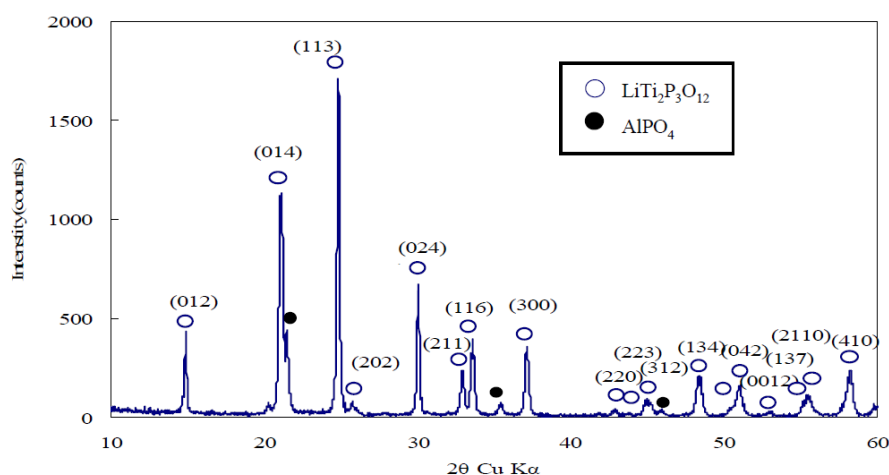


**Figure 5-3.** XRD results of LiCGC inorganic plate from the Ohara incorporation.

The [gel | LiCGC | gel] sandwich structure electrolyte was assembled in an Ar-filled glove box with SUS blocking electrode, where Li ions must pass through the LiCGC plate and the contact area of the electrode/ electrolyte was 16 mm diameter (**Figure 5-4**).<sup>8-11</sup> The impedance was measured with an impedance analyzer (Biologic, VMP3) in the frequency range of 1 MHz to 100 mHz and various temperature range with an amplitude of 10 mV. Activation energy for Li ion transfer was calculated according to Arrhenius equation.

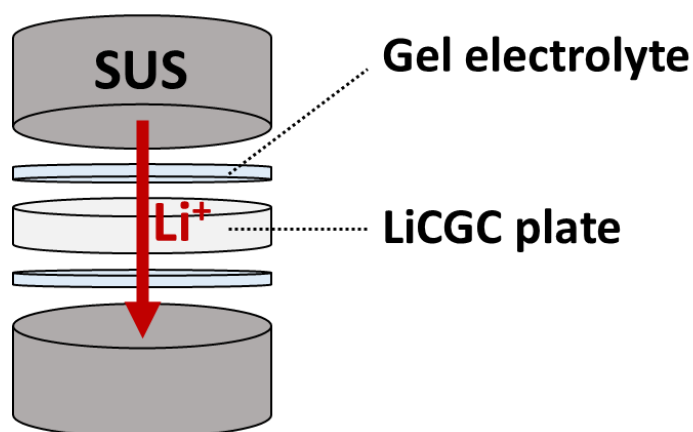


**Figure 5-4.** A schematic image of gel/Ohara/gel sandwich cell.

### 5.3.2 Quantify the interfacial resistance of composite electrolyte

To investigate the rate of  $\text{Li}^+$  exchange at the interface between the gel electrolyte and LATP, a symmetric cell of [SUS/gel/LATP plate/gel/SUS] was assembled using an LATP plate (LiCGC, Ohara Inc.), and AC impedance measurements were conducted. LiCGC is a commercially available LATP plate and has a relatively high ionic conductivity of  $1.16 \times 10^{-4} \text{ S cm}^{-1}$  at  $30^\circ\text{C}$  (**Figure 5-5b**).

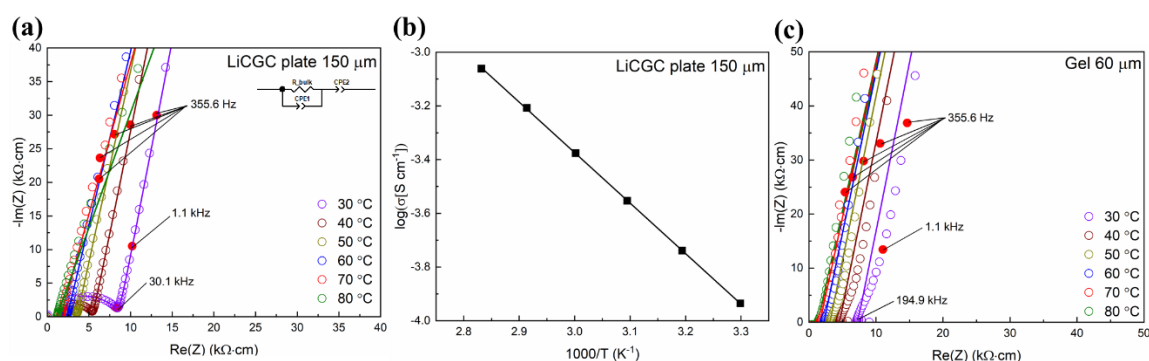


**Figure 5-5.** (a) Nyquist plots and (b) ionic conductivity of the LiCGC plate measured at various temperatures. Au is coated on both sides of the LATP plate using a sputtering method, and the AC impedance is measured. (c) Nyquist plots of PVDF–HFP gel measured at various temperatures.

**Figure 5-6a** shows the Nyquist plots of the symmetric cell measured at various temperatures. A depressed semicircle was observed in the high-frequency region ( $>10 \text{ kHz}$ ), and a sloping line appeared at frequencies lower than  $10 \text{ kHz}$ . **Figure 5-6b** shows the equivalent circuit model for the SUS/Gel/SE/Gel/SUS cell. The depressed semicircle in the high-frequency region is assumed to originate from the resistances of the LiCGC plate ( $R_{LATP}$ ), the gel electrolyte ( $R_{gel}$ ), and the interfacial resistance between the LiCGC and the PVDF–HFP gel ( $R_{int}$ ). The diameter of the semicircle,  $R_{tot}$ , is the sum of  $R_{LATP}$ ,  $R_{gel}$ , and  $R_{int}$ . We could not distinguish  $R_{LATP}$ ,

$R_{gel}$ , and  $R_{int}$ , because the time constants of the interfacial  $\text{Li}^+$  transfer process at LATP/gel and ion conduction in the LATP and PVDF–HFP gels were similar. Therefore, AC impedance measurements were conducted on the LICGC plate and gel electrolyte sheet separately, and their resistivities were evaluated (**Figure 5-5**). From the resistivities, the resistances  $R_{LATP}$  and  $R_{gel}$  in the three-layer gel/SE/gel electrolyte cell were calculated, and the interfacial resistance  $R_{int}$  was estimated as follows:  $R_{int} = R_{tot} - R_{LATP} - R_{gel}$ . **Figure 5-6c** shows the Arrhenius plot of  $1/R_{int}$ , where the Li-ion transfer rate at the interface is proportional to  $1/R_{int}$ . The  $R_{int}$  value is the sum of the two interfacial resistances of gel/LICGC/gel, and the normalized interfacial impedance of a single interface of LICGC/gel was  $67 \text{ } \Omega \text{ cm}^2$  at  $30 \text{ } ^\circ\text{C}$ . The activation energy for the charge transfer (i.e., Li-ion transfer) at the interface of the LICGC/gel was estimated to be  $39 \text{ kJ mol}^{-1}$ , whereas the activation energies of ion conduction in LICGC and PVDF–HFP gel were  $36 \text{ kJ mol}^{-1}$  and  $32 \text{ kJ mol}^{-1}$ , respectively. As discussed previously,  $\text{Li}^+$  conduction in the LATP gel composite electrolyte mainly occurs in the gel phase. The passage through the interface of the LATP/gel is unfavorable for  $\text{Li}^+$  ion conduction in the composite electrolyte because of the interfacial resistance of LATP/gel and the activation barrier for interfacial Li-ion transfer. Although we cannot conclude what determines the Li-ion transfer rate at the LATP/gel interface currently, the interaction between  $\text{Li}^+$  and ligands (solvent and anion) in the gel electrolyte and the interaction between  $\text{Li}^+$  and anions in LATP would certainly affect the Li-ion transfer process because the environment of  $\text{Li}^+$  in the gel electrolyte and the LATP should be significantly different. To achieve a higher Li-ion transfer rate (or lower  $R_{int}$ ), further investigations are required.

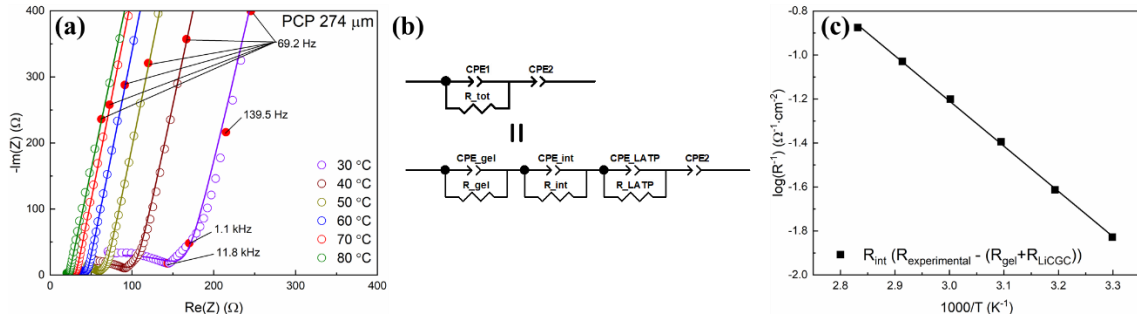


**Figure 5-6.** (a) Nyquist plots of an SUS/gel/LiCGC/gel/SUS cell measured at various temperatures. The area of each gel electrolyte is 2 cm<sup>2</sup>, and the total thickness of the two gel electrolytes is 124 μm. The area of the LiCGC plate is 2 cm<sup>2</sup> with a thickness of 150 μm. (b) Equivalent circuit model of the SUS/gel/SE/gel/SUS cell. Constant phase elements (CPEs) are used instead of capacitances to fit the impedance spectra. (c) Arrhenius plot of 1/*R<sub>int</sub>*. *R<sub>int</sub>* is normalized using the contact area (2 cm<sup>2</sup>) of the LiCGC/gel electrolyte and divided by 2 (number of interfaces).

## 5.4 Conclusions

In this work, flexible composite electrolytes comprising LATP powder and PVDF–HFP gel containing [Li(SL)<sub>2</sub>][TFSA] were prepared using a solution casting method. Li/LiCoO<sub>2</sub> cells could be operated successfully with a composite electrolyte; however, the rate capability of the cell degraded with increasing LATP content in the composite electrolyte. The ionic conductivity of the composite electrolyte decreased with increasing LATP content. In the composite electrolytes, the gel formed a continuous phase, and Li-ion conduction mainly occurred in the gel phase. The LATP particles contributed less to Li-ion conduction in the composite electrolytes. This was attributed to the resistance to Li<sup>+</sup> transfer at the interface between the LATP and PVDF–HFP gels. The interfacial resistance of the LATP/gel was 67 Ω cm<sup>2</sup> at 30 °C, and the activation energy for interfacial Li<sup>+</sup>

transfer was estimated to be 39 kJ mol<sup>-1</sup>. The passage through the interface of the LATP/gel is unfavorable for Li ion conduction in the composite electrolyte because of the interfacial resistance of LATP/gel and the activation barrier for interfacial Li ion transfer.

## 5.5 References

- 1 N. Nitta, F. Wu, J. T. Lee and G. Yushin, *Mater. Today*, 2015, **18**, 252–264.
- 2 S. Wenzel, T. Leichtweiss, D. Krüger, J. Sann and J. Janek, *Solid State Ionics*, 2015, **278**, 98–105.
- 3 T. Nakamura, K. Amezawa, J. Kulisch, W. G. Zeier and J. Janek, *ACS Appl. Mater. Interfaces*, 2019, **11**, 19968–19976.
- 4 Y. Zhu, X. He and Y. Mo, *ACS Appl. Mater. Interfaces*, 2015, **7**, 23685–23693.
- 5 P. Hartmann, T. Leichtweiss, M. R. Busche, M. Schneider, M. Reich, J. Sann, P. Adelhelm and J. Janek, *J. Phys. Chem. C*, 2013, **117**, 21064–21074.
- 6 J. C. Bachman, S. Muy, A. Grimaud, H. H. Chang, N. Pour, S. F. Lux, O. Paschos, F. Maglia, S. Lupart, P. Lamp, L. Giordano and Y. Shao-Horn, *Chem. Rev.*, 2016, **116**, 140–162.
- 7 M. Kotobuki and M. Koishi, *Ceram. Int.*, 2013, **39**, 4645–4649.
- 8 W. Zhou, S. Wang, Y. Li, S. Xin, A. Manthiram and J. B. Goodenough, *J. Am. Chem. Soc.*, 2016, **138**, 9385–9388.
- 9 F. Langer, M. S. Palagonia, I. Bardenhagen, J. Glenneberg, F. La Mantia and R. Kun, *J. Electrochem. Soc.*, 2017, **164**, A2298–A2303.
- 10 B. Liu, Y. Gong, K. Fu, X. Han, Y. Yao, G. Pastel, C. Yang, H. Xie, E. D. Wachsman and L. Hu, *ACS Appl. Mater. Interfaces*, 2017, **9**, 18809–18815.
- 11 X. C. Chen, X. Liu, A. S. Pandian, K. Lou, F. M. Delnick and N. J. Dudney, *ACS Energy Lett.*, 2019, **4**, 1080–1085.

## **Chapter Six**

Concluding remarks and future directions

## 6. Concluding remarks and future directions

In this study, a flexible gel polymer membrane is developed by combining a PVDF-HFP and SL based highly concentrated electrolyte. In SL based highly concentrated electrolyte,  $\text{Li}^+$  ions diffuse faster than solvents and anions, where two oxygen atoms of the sulfonyl groups coordinate to Li ions and formed chainlike Li-ion coordination structures, as reflected by the fastest  $\text{Li}^+$  ion diffusion among the electrolyte components. The Raman spectra of  $[\text{Li}(\text{SL})_2][\text{TFSA}]$  gel membrane was in a similar shape to the corresponding Raman spectra of parent ionic liquid, indicating that there is a minor interaction between polymer matrix and highly concentrated electrolyte. The prepared SL based gel electrolytes showed sufficient Li ion conducting properties as contained highly concentrated liquid electrolytes applicable to lithium-ion batteries. The anionic effect of the SL-based gel electrolytes on the Li ion conductivity and charge transfer kinetics at the gel/electrode interface was investigated. Among these, Li/LiCoO<sub>2</sub> cell with the  $[\text{Li}(\text{SL})_3][\text{FSA}]$  gel electrolyte showed a good capacity retention with a high coulombic efficiency under high discharge current density, which is assumed to the suppression of the concentration gradient development in the cell.

In an effort to achieve fast  $\text{Li}^+$  ion conductive gel, a composite electrolyte was prepared by combining LATP and PVDF-HFP gel electrolyte. The membrane was self-standing and flexible. <sup>6</sup>Li MAS-NMR measurement revealed that Li ion exchange reaction occurred in the composites, suggesting that both LATP and organic components contribute to the Li ion conduction in the composite electrolyte. However, a higher content of LATP leads to an increase in interfacial resistance of the composite electrolytes, which in turn decreases the battery performance. In the composite electrolytes, gel formed a continuous phase and Li-ion conduction mainly occurred in the gel phase. Additionally, the large interfacial resistance was found at the LATP/gel was 67  $\Omega \text{ cm}^2$  at 30 °C, which contributed to less Li-ion conduction in the LATP particles. These results, bringing about an

issue in composite electrolyte, where interfacial resistance of different components should be low enough to actively exchange the mobile ions to uniformly distribute to the electrochemical properties and get the synergetic effect.

Herein, the electrochemical properties and correlations of solid electrolytes combining the different phases of electrolytes were proposed in this paper, which could enhance the power performance of Li-ion battery. It is expected that solid electrolyte could be strong growth in the field of electrolyte as they have potential to remedy each component and improve the safety and cell performance. However, in order to replace the conventional organic electrolytes, intensive efforts should be made in solid electrolyte to address the issues at the interface. Understanding the factors affecting Li-ion transfer at the interface in composite electrolyte is essential in achieving the mutual compensation so it could expand the practical application in Li-ion battery.

## Publication list

**J.Y. Ock**, M. Fujishiro, K. Ueno, I. Kawamura, R. Tatara, K. Hashimoto, M. Watanabe, and K. Dokko, Transport Properties of Flexible Composite Electrolytes Composed of  $\text{Li}_{1.5}\text{Al}_{0.5}\text{Ti}_{1.5}(\text{PO}_4)_3$  and Poly(vinylidene fluoride-*co*-hexafluoropropylene) Gel Containing a Highly Concentrated  $\text{Li}[\text{N}(\text{SO}_2\text{CF}_3)_2]$ /Sulfolane Electrolyte. *ACS Omega*, 2021, 6, 16187–16193.

**J.Y. Ock**, M. Fujishiro, K. Ueno, M. Watanabe, and K. Dokko, Electrochemical Properties of Poly(vinylidene fluoride-*co*-hexafluoropropylene) Gel Electrolytes with High-Concentration Li Salt/Sulfolane for Lithium Batteries. *Electrochemistry*, 2021, in press